

Phase-field study of surface diffusion enhanced break-ups of nanowire junctions

Abhinav Roy,¹ Arjun Varma R.,² and M. P. Gururajan²

¹*Department of Metallurgical and Materials Engineering,
National Institute of Technology Rourkela, Odisha, 769008 INDIA*

²*Department of Metallurgical Engineering and Materials Science,
Indian Institute of Technology Bombay, Powai, Mumbai, Maharashtra,
400076 INDIA*

(*Electronic mail: gururajan.mp@gmail.com; guru.mp@iitb.ac.in)

Using a phase-field model which incorporates enhanced diffusion at the nanowire surfaces, we study the effect of different parameters on the stability of intersecting nanowires. Our study shows that at the intersection of nanowires, sintering (curvature driven material flow) leads to the formation of junctions. These junctions act the initiators of nanowire break-up. The subsequent break-ups take place due to Rayleigh instability at the arms away from these junctions. Finally, at long time scales, the fragments coarsen due to the differences in sizes. The radii of the nanowires that form the junction, the difference in size of the intersecting nanowires and the angle of intersection play a dominant role in determining the kinetics of break-up while the density of intersections has little or no effect on the kinetics. We rationalise our results using maps of (i) mean curvatures (and, hence, chemical potentials), and, (ii) Interfacial Shape Distributions (ISDs) (which are based on probability densities associated with different combinations of the two principal curvatures). Finally, we use the moment of inertia tensor to characterise the (non-spherical) shapes and morphologies of (central) nanowire fragments at the junctions.

I. INTRODUCTION

Metallic nanowires are used in a wide range of applications: for example, their ductility and bendability allows for their use in solar cells, flexible and transparent electronic devices, light emitting diodes, and so on – see, for example,^{1–4}. Regular ordered array of metallic nanodots have been used in biosensing applications⁵. In particular, network of Ag nanowires are considered as the next generation of transparent conducting electrodes due to their enhanced electrical and optical properties^{6,7}. Given such widespread use, their stability at elevated temperatures under standard operating conditions is an important area of study. Thus, an understanding of the driving forces for morphological changes and control of the parameters which affect those driving forces are of significant academic and technological importance.

The effect of nanowire size, network density and temperature on the stability of metallic nanowires have been investigated experimentally^{8–10}. The structural stability of the metallic nanowires at the nanoscale is governed by numerous factors — the most dominant factors being Rayleigh instability^{11–13} and anisotropy in interfacial energy^{14–18}. Thermally accelerated surface diffusion plays a central role in the resulting change in morphology of the metallic nanowires due to Rayleigh instability, and their subsequent break-up into nanodots^{19–25}. Rayleigh instability mediated nanowire fragmentation has also been observed in non-metallic nanowires^{26,27}. Quantum effects at the nanoscale also play a role in morphological evolution in conjunction with Rayleigh instability and have been investigated both experimentally and numerically^{28,29}.

It has been observed experimentally that nanowire junctions have a drastic effect on the break-up kinetics of Au and Ag nanowires when annealed at elevated temperatures much below their melting point³⁰. Presence of such junctions between the nanowires lead to initial break-up preferentially at the junction, followed by break-up at remainder of the nanowires. Such fragmentation behaviour of nanowires can be exploited to produce ordered array of nanodots for different technological applications^{31,32}.

In the past, various modelling approaches (mostly atomistic) have been adopted to simulate the nanoparticle morphologies and various effects at the nanoscale — a review of such approaches can be found in³³ and references therein. Linear stability analysis of Rayleigh instability is also well understood; for example, a linear stability analysis of the effect of general surface energy anisotropy on Rayleigh instability has been carried out in¹⁶ (extending the work of Cahn¹⁴).

Phase-field modelling is an efficient numerical technique for simulating microstructural evo-

lution at the mesoscopic length scales and diffusive time scales^{34,35}. There exist several phase-field models to study variable mobility; for example, variable mobilities have been introduced in the past to study phenomena such as domain growth in binary mixtures³⁶, late-stage coarsening in phase separating systems^{37,38}, and for determining the coarsening kinetics of bulk-diffusion-controlled and interface-diffusion-controlled growth in systems with interconnected phases³⁹. The use of variable mobility phase-field models has also been made for effectively incorporating the effect surface diffusion, assuming isotropic interfacial energy^{40–42}. Such variable mobility phase-field models have been used in simulating the Rayleigh instability in the solid-state⁴³, destabilisation of nanoporous membranes by grain boundary grooving⁴⁴, thermal stability of nanoporous aggregates⁴⁵, and, instability in multi-layer nanocrystalline thin-films due to Rayleigh instability driven by grain boundary⁴⁶.

Phase-field models have been developed to incorporate anisotropy in interfacial energy using either trigonometric functions for the interfacial energy coefficient^{47,48}, or using higher order tensor terms which has benefits over the former approach⁴⁹. Phase-field model for stability of nanowire fragmentation with regularized trigonometric function of interfacial energy along with finite amplitude axisymmetric perturbations has been developed previously⁵⁰. Higher order tensor terms in the free energy functional of phase-field models have been used to study the faceting of precipitates due to interfacial energy anisotropy⁵¹.

Our aim, in this paper, is to implement a continuum model (based on the Cahn-Hilliard equation⁵²) for long time evolution of the morphologies of the nanowires with enhanced surface diffusion. Further, the formulation and its implementation are capable of accommodating surface energy anisotropy. Specifically, we use the extended Cahn-Hilliard equation which consists of a fourth order tensor term in order to incorporate cubic surface energy anisotropy, and, following the approach adopted in some of the previous phase-field studies mentioned above, we define an order-parameter dependent mobility function. This helps us incorporate enhanced surface diffusion in our model. Using this model, we carry out a systematic study of various factors such as wire diameters, the angles of intersection, and density of intersections in the simulation cell on fragmentation of intersecting nanowires; our preliminary, 2-D results on the effect of anisotropy are given as an appendix.

At this point, we want to note that there exist phase-field studies pertaining to the phenomena of solid-state dewetting in nanowires^{17,53,54}. Different phenomena like the formation of nanoparticles through solid-state dewetting of a thin-film on a substrate⁵⁵, stress effects on solid-state dewetting

of thin-films⁵⁶, solid-state dewetting of Au aggregates on titanium oxide nanorods⁵⁷, and effect of surface energy anisotropy on Rayleigh-like solid-state dewetting¹⁷ have been studied in the past. Note that there is also the possibility of Asaro-Tiller-Grinfeld instabilities in nanowires on substrates – see, for example⁵⁸. However, unlike these models which include the substrate on which dewetting takes place, in our model, the wires are free-standing.

The rest of this paper is organized as follows: we describe (albeit briefly) the formulation and numerical implementation of the phase-field model in section II, which also contains the simulation details. Results and discussion follow in section III where we discuss the effect of various parameters on the kinetics of junction break-up systematically, followed by a discussion on the morphology of the fragments IV; we conclude the paper with a summary of our salient conclusions in section V.

II. PHASE-FIELD MODEL

As indicated in the introduction, our phase-field model is a combination of extended Cahn-Hilliard model for cubic anisotropy in interfacial energy⁴⁹ coupled with enhanced surface diffusion implemented using a variable mobility³⁹. Since these models are well known in the literature, we briefly describe the models and other details in this section, for the sake of completion.

A. Formulation

We consider a conserved, non-dimensionalised order parameter, denoted by $c(x, t)$ to describe our system. This order parameter takes a value of zero in vacuum and unity in the (nanowire) material albeit across a flat interface; in the circular cross-section nanowire-vacuum geometry, the order parameter value shifts from unity and zero to account for Gibbs-Thomson effect.

The free energy functional of the system is given by the expression:

$$F = N_V \int_{\Omega} \left\{ f_0(c) + \frac{\kappa_c}{2} (|\nabla c|)^2 + \frac{\gamma_{\langle hkl \rangle}}{2} (\nabla^2 c)^2 \right\} d\Omega, \quad (1)$$

where, N_V denotes the number of atoms per unit volume (assumed to be constant), $f_0(c)$ is the bulk free energy density per atom, κ_c is the gradient energy coefficient (assumed to be a scalar and hence gives rise to an isotropic interfacial free energy), and, the third term accounts for cubic interfacial free energy anisotropy as explained below.

The cubic anisotropy in the interfacial energy of the nanowires is incorporated into the model using the extended Cahn-Hilliard formulation⁴⁹, which is the third term in the equation. In Eq. 1, $\gamma_{\langle hkl \rangle}$ is the coefficient of a fourth order term which is defined for a particular crystallographic orientation as:

$$\gamma_{\langle hkl \rangle} = \gamma_I + \gamma_A (h^4 + k^4 + l^4), \quad (2)$$

where, γ_A and γ_I are the anisotropic and isotropic contributions from the fourth rank term, and h, k, l denote the Miller Indices of the normal to the interface. Abinandanan and Haider⁴⁹ have also shown that the interfacial energy scales as $\gamma_{\langle hkl \rangle}^{\frac{1}{4}}$. The values of γ_A and γ_I can be chosen using the scaling curve given by Abinandanan and Haider⁴⁹, and knowing the ratio of interfacial energies along different directions.

In Eq. 1, the function $f_0(c)$ represents the bulk free energy density per atom, which is given by the polynomial,

$$f_0(c) = A_c [c^2(1-c)^2]. \quad (3)$$

This polynomial produces a double well potential with the energy minima at $c = 0$ (vacuum) and $c = 1$ (nanowire material). A_c is a coefficient that determines the height of the potential energy barrier. Together with the gradient energy coefficient κ_c , A_c determines the interfacial energy and width in the system (in the absence of the $\gamma_{\langle hkl \rangle}$ term; when present, $\gamma_{\langle hkl \rangle}$ along with A_c and κ_c determine the interfacial properties, namely, energy and width).

The chemical potential is derived from the variational derivative of the free energy functional Eq.1:

$$\mu = \frac{1}{N_V} \frac{\delta F}{\delta c} = \left[\frac{\partial f_0(c)}{\partial c} - \kappa_c \nabla^2 c + \gamma_{\langle hkl \rangle} \nabla^4 c \right]. \quad (4)$$

The evolution of the system is described by the modified Cahn-Hilliard equation, which is given by the expression:

$$\frac{\partial c}{\partial t} = \nabla \cdot [M(c) \cdot \nabla (f_0(c) - \kappa_c \nabla^2 c + \gamma_{\langle hkl \rangle} \nabla^4 c)], \quad (5)$$

where, $M(c)$ denotes the mobility as a function of the order parameter, and is used to capture the effect of surface diffusion.

Various polynomials have been suggested in the literature for use as variable mobility functions in the Cahn-Hilliard equation. Most commonly used mobility functions in previous studies have been quadratic and quartic function⁵⁹⁻⁶³ of order parameter, to incorporate the dominating role of surface diffusion in the models. The mobility function used in our model serves the same purpose,

and has an added advantage of reducing the stiffness of the equations in conjunction with the semi-implicit Fourier spectral numerical method. The function is defined as follows:

$$M(c) = [c(1-c)]^{\frac{1}{2}}. \quad (6)$$

Substituting Eq. 6 into Eq. 5, the evolution equation can be written as:

$$\frac{\partial c}{\partial t} = \nabla \cdot \left[\{c(1-c)\}^{\frac{1}{2}} \cdot \nabla \left(\frac{\partial f_0(c)}{\partial c} - \kappa_c \nabla^2 c + \gamma_{\langle hkl \rangle} \nabla^4 c \right) \right]. \quad (7)$$

Note that the polynomial (6) gives the maximum mobility along the surface of the wire ($c = 0.5$) and is zero within the nanowire ($c = 1$) and outside it ($c = 0$). Thus, in these simulations, surface diffusion plays a dominant role in material transport. In order to make sure that zero mobility in the bulk and vacuum does not produce any numerical instabilities, we have carried out simulations taking the bulk and vacuum mobilities to be two orders of magnitude less than that of surface mobility; we have found that the time for the first pinch-off at the junction remains the same in both these cases: see the Supplementary Information.

B. Numerical implementation

The evolution equation (Eq. 7) is solved numerically in order to track the morphological evolution of both finite and infinite cylindrical nanowires (in both 2-D and 3-D). We use the semi-implicit Fourier spectral technique for solving the evolution equation. This method is known to be efficient for solving non-linear partial differential equations and also eliminates the severe time-step constraint^{39,64}. We follow the same method of discretisation used in³⁹. We transform equation Eq. 7 to Fourier space and perform first order forward finite-difference discretisation in time.

$$\frac{\tilde{c}(\mathbf{k})^{t+\Delta t} - \tilde{c}(\mathbf{k})^t}{\Delta t} = i\mathbf{k} \{ \{c(1-c)\}^{\frac{1}{2}} \cdot [i\mathbf{k}' (\tilde{g}(c^t) + \tilde{c}(\mathbf{k}')^t \chi)]_r \}_k, \quad (8)$$

where, i is the pure imaginary number,

$$\chi = (\kappa_c k'^2 + \gamma_I k'^4 + \gamma_A (k_x'^4 + k_y'^4 + k_z'^4)),$$

$\tilde{c}(\mathbf{k}, t)$ is the non-dimensionalised order parameter field in the Fourier space and, \mathbf{k} and \mathbf{k}' are the Fourier space vectors. $|\mathbf{k}| = k = \sqrt{k_x^2 + k_y^2 + k_z^2}$, where k_x , k_y and k_z are the three components of the Fourier space vector. The operation $[\cdot]_r$ represents the inverse spatial Fourier transform of

the quantity in square brackets to the real space, while $\{\cdot\}_k$ represents the forward spatial Fourier transform of the quantity in curly brackets. The function $g(c)$ represents the derivative of the bulk free energy density function with respect to c and is defined as:

$$g(c) = \frac{\partial f_0(c)}{\partial c} = 2A_c \{c(1-c)(1-2c)\}. \quad (9)$$

The severe time step constraint associated with the explicit solution of the equation is circumvented by introducing a suitable stabilizing constant, which separates the mobility function into two parts: ξ and $\{c(1-c)\}^{\frac{1}{2}} - \xi$, after Zhu et al.³⁹. Therefore, the modified evolution equation becomes:

$$\frac{\tilde{c}(\mathbf{k})^{t+\Delta t} - \tilde{c}(\mathbf{k})^t}{\Delta t} = i\mathbf{k} \left\{ \left[\xi + \left\{ c(1-c) \right\}^{\frac{1}{2}} - \xi \right] \cdot [i\mathbf{k}'(\tilde{g}(c^t) + \tilde{c}(\mathbf{k}')^t \chi)]_r \right\}_k. \quad (10)$$

It is known that the choice of ξ that lies in the middle of the maximum and minimum values of the mobility gives the best performance for the numerical scheme³⁹. Hence, in these simulations, we have taken ξ as $\frac{1}{2}(\max[M(c)] + \min[M(c)]) = \frac{1}{2}(0.5 + 0) = 0.25$.

After some algebraic manipulation, the evolution equation can be written as:

$$\beta \tilde{c}(\mathbf{k})^{t+\Delta t} = \beta \tilde{c}(\mathbf{k})^t + i\mathbf{k}\Delta t \{c(1-c)\}^{\frac{1}{2}} \cdot [i\mathbf{k}'(\tilde{g}(c^t) + \tilde{c}(\mathbf{k}')^t \chi)]_r \}_k \quad (11)$$

where, $\beta = (1 + \xi \Delta t \chi)$.

Thus, knowing the c at a given time t , the c at time $t + \Delta t$ can be obtained in the Fourier space using Eq. 11.

C. Simulation details

We have carried out simulations of finite and infinite nanowires in both 2- and 3-D. In this paper, we present 3-D results for wires with isotropic interfacial energy (and 2-D results for wires with (cubic) anisotropic interfacial energy, in the Appendix A.). The deployment of Fourier spectral technique for the numerical solution implies imposition of periodic boundary conditions. We introduce a small noise in the scaled order parameter, which adequately simulates the thermal noise in the system. We used the software package Fastest Fourier Transform in the West (FFTW3)⁶⁵ for computing the discrete Fourier transforms. We use the same non-dimensionalisation as described in Abinandanan and Haider⁴⁹. The non-dimensional simulation parameters used in our simulations are tabulated in Table I. Note that the lengths are reported in units of grid lengths for the rest of this paper; that is, an R value of 16 corresponds to a non-dimensional length of 8 in the 3-D isotropic case, and so on.

TABLE I. Non-dimensional simulation parameters

| Simulation Case | Simulation Parameters | Values |
|-------------------------------------|----------------------------------|----------------------------|
| General parameters | κ_c | 1.0 |
| | A_c | 1.0 |
| | ξ | 0.5 |
| Isotropic interfacial energy case | $N_x \times N_y \times N_z$ (3D) | $768 \times 768 \times 96$ |
| | $\Delta x = \Delta y = \Delta z$ | 0.5 |
| | Δt | 1.0 |
| | $\gamma_I = \gamma_A$ | 0 |
| Anisotropic interfacial energy case | $N_x \times N_y$ (2D) | 512×512 |
| | $\Delta x = \Delta y$ | 1.0 |
| | Δt | 0.01 |
| | γ_I | -50^{66} |
| | γ_A | 107.69^{66} |

III. RESULTS AND DISCUSSION

The angle of intersection of the nanowires, the radii of the nanowires and the size difference in the radii between the nanowires that form the intersections, and the density of intersections are the parameters that are of interest to us. In this section, we present our results for all these scenarios. Before we do so, in order to benchmark our implementation, we first present results from single nanowire simulations and show that the results are in good agreement with known analytical results for Rayleigh instability in infinite rods.

A. Single nanowire simulations

We have carried out simulations on free standing single finite and infinite nanowires of radii of 12, 13, 14, 15, and 16 in 3D. The interfacial energy in all these cases is isotropic. The morphological snapshots for radius 12 nanowire for both finite and infinite cases are shown in Fig. 1. The morphological evolution for the other radii are given in the supplementary information.

From the morphological snapshots at different timesteps it can be seen that the wires fragment

from the edges in the case of a finite wire. The free ends retract, and bulge to form constrictions along the body of the nanowires, which lead to further break-up. In the case of infinite nanowires, the perturbations set in and lead to break-up of nanowire into fragments; the first break-up, however, in contrast to finite nanowire, occurs at a random location along the body of the nanowire.

It is well known in the literature that in case of infinite solid cylindrical rods with isotropic surface energy, the fragment separation is dominated by the maximally growing wavelength (λ_{max}). This maximally growing wavelength is related to initial radius of the cylinder as $\lambda_{max} = 8.89R$ (See Ref.^{20,67}) in case of purely surface diffusion mediated instability. From this expression, the average separation between nanoparticles formed after fragmentation should be 106.68 and 124.46 units for radius 12 and 14, respectively. It is observed from simulations that when the fragmentation starts, the average separation between particles in case of radius 12 is about 108 ± 19 and in case of radius 14 is about 129 ± 54 – indicating that the separation between the fragmented nanoparticles in our simulations is broadly consistent with the maximally growing wavelength obtained from the analytical expressions for Rayleigh instability. The large error bars are because of subsequent break-ups and coarsening of the initial fragments.

In order to confirm that it is the Rayleigh instability that causes for nanowire fragmentation in our simulations, we have plotted the time for first pinch-off t_f against R^4 in Fig. 2. We fit a straight line of the form $R^4 = mt_f$ using non-linear least squares method to the data points. The value of slopes are: $m = 5.34 \pm 0.33$ ($R^2 = 0.98$) for the infinite wire. In the case of the finite wire, $m = 7.07 \pm 0.30$ ($R^2 = 0.99$). As seen in the figure, the fit is good and in line with the expectation from theoretical studies of surface diffusion mediated Rayleigh instability¹².

Finally, using these single wire simulations, we also calculate the change composition due to the Gibbs-Thomson effect. For our case, where the equilibrium compositions of the nanowire and the vacuum across a planar interface is kept at unity and zero respectively, this change is given by (see, for example, Appendix E of Ref.⁶⁸)

$$\Delta c = \frac{\chi\gamma}{\frac{\partial^2 f_0}{\partial c^2}} \quad (12)$$

In this equation, Δc is the difference between the equilibrium composition for a flat interface and the curved interface with mean curvature χ ; the mean curvature of the interface ($\chi = 1/R$), where R is the instantaneous radius of the nanowire; γ is the interfacial free energy and the denominator is the second derivative of the bulk free energy density evaluated at the equilibrium composition. The (scaled) interfacial energy (γ) in our model takes a value of 0.33. The second derivative of free

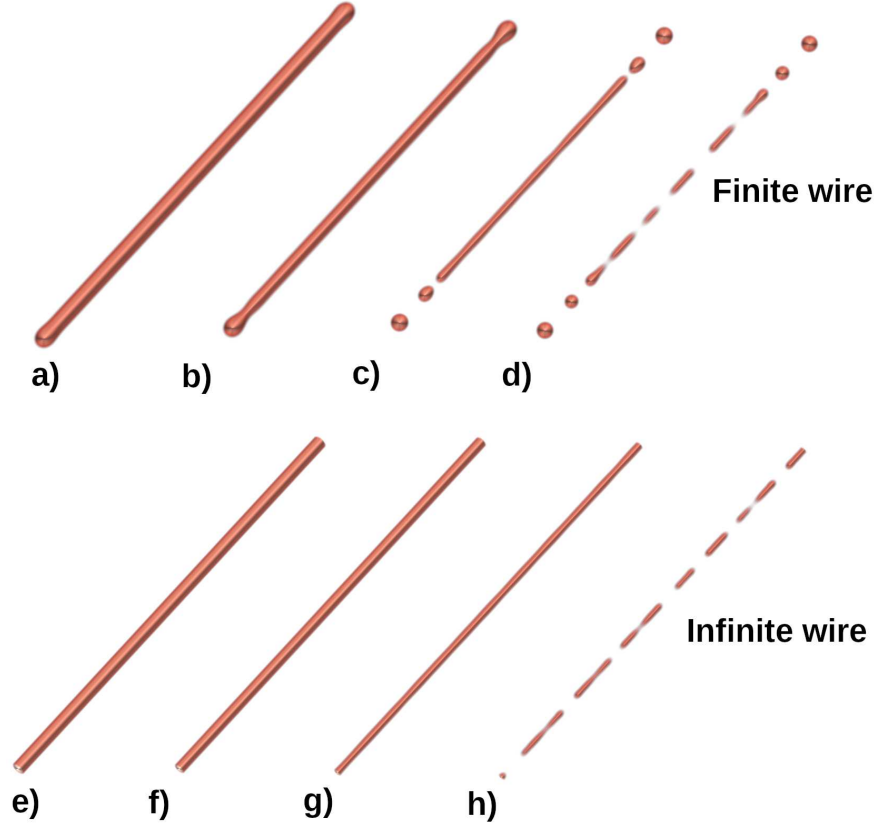


FIG. 1. Single nanowire simulations for finite nanowires of radius 12 at (a) $t=500$ (b) $t=1500$ (c) $t=2700$ (d) $t=2800$ and infinite nanowires at (e) $t=500$ (f) $t=1500$ (g) $t=2700$ (h) $t=2800$ respectively.

energy in our model takes a value of 2. Using these values, for a single nanowire of radius 16, the change in composition (Δc) is analytically evaluated to be $\Delta c = 0.0175$ and we obtain a Δc of 0.017 from our simulations. Similarly, for a nanowire of radius 12, the analytically calculated value is $\Delta c = 0.018$ and in our simulations of 90° configuration with radii 12 for both the nanowires, we see $\Delta c = 0.019$. Thus, our phase field model accurately captures the change in composition in the system due to Gibbs-Thomson effect.

B. Effect of relative orientation

We consider a system with isotropic interfacial energy (in 3D) with a single intersection of the nanowires (of circular cross-section) in the simulation cell. We assume periodic boundary conditions. As seen from the schematic top view of the relative orientations in Fig.3, in the case of an intersection angle of 90° , both the wires are infinite. However, for all the other three angles,

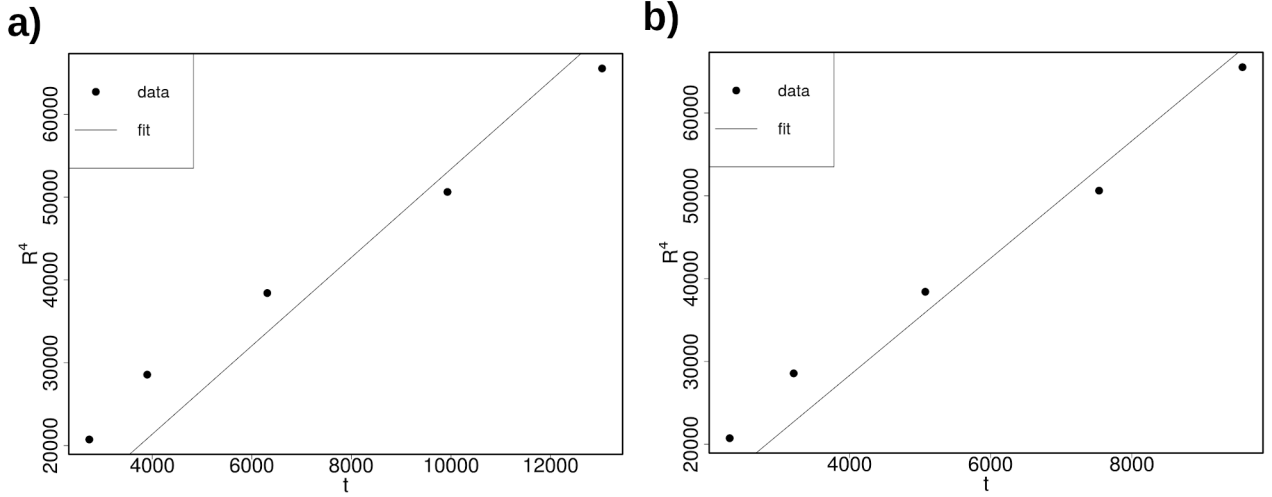


FIG. 2. The plot of first pinch-off time (t_f) against R^4 . We fit a line ($R^4 = mt_f$) using non-linear least squares method to the data points. The value of slopes are: $m = 5.34 \pm 0.33$ ($R^2 = 0.98$) for the infinite wire. In the case of the finite wire, $m = 7.07 \pm 0.30$ ($R^2 = 0.99$).

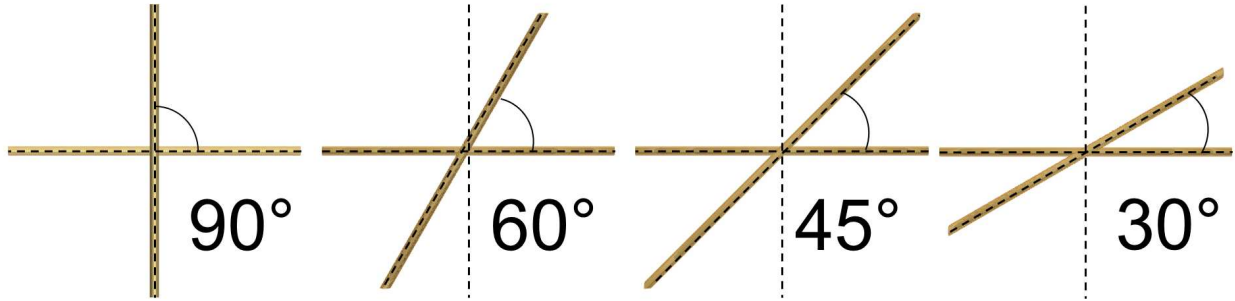


FIG. 3. Schematic (top view) of the relative orientation between the wires used in the current study

the nanowire parallel to the x -axis of the simulation cell is infinite while the other one is finite. Having said that, we have chosen big enough system sizes so that the break-up at the edges of the finite nanowire does not affect the break-up at the intersection.

In Fig.4, we show the time evolution of the nanowires of equal initial radii ($R_1 = R_2 = 12$ (non-dimensional) length units) with an angle of 90° at the intersection to begin with. Note that in 3D, one nanowire (in this case, the one along the x -axis) is at the bottom and the other on top (in this case, the one along the y -axis); in this and the subsequent cases, R_1 represents the radius of the nanowire at the bottom and R_2 represents the radius of the nanowire on top. As can be seen from the figure, due to the high curvatures at the point of contact at the intersection, initially,

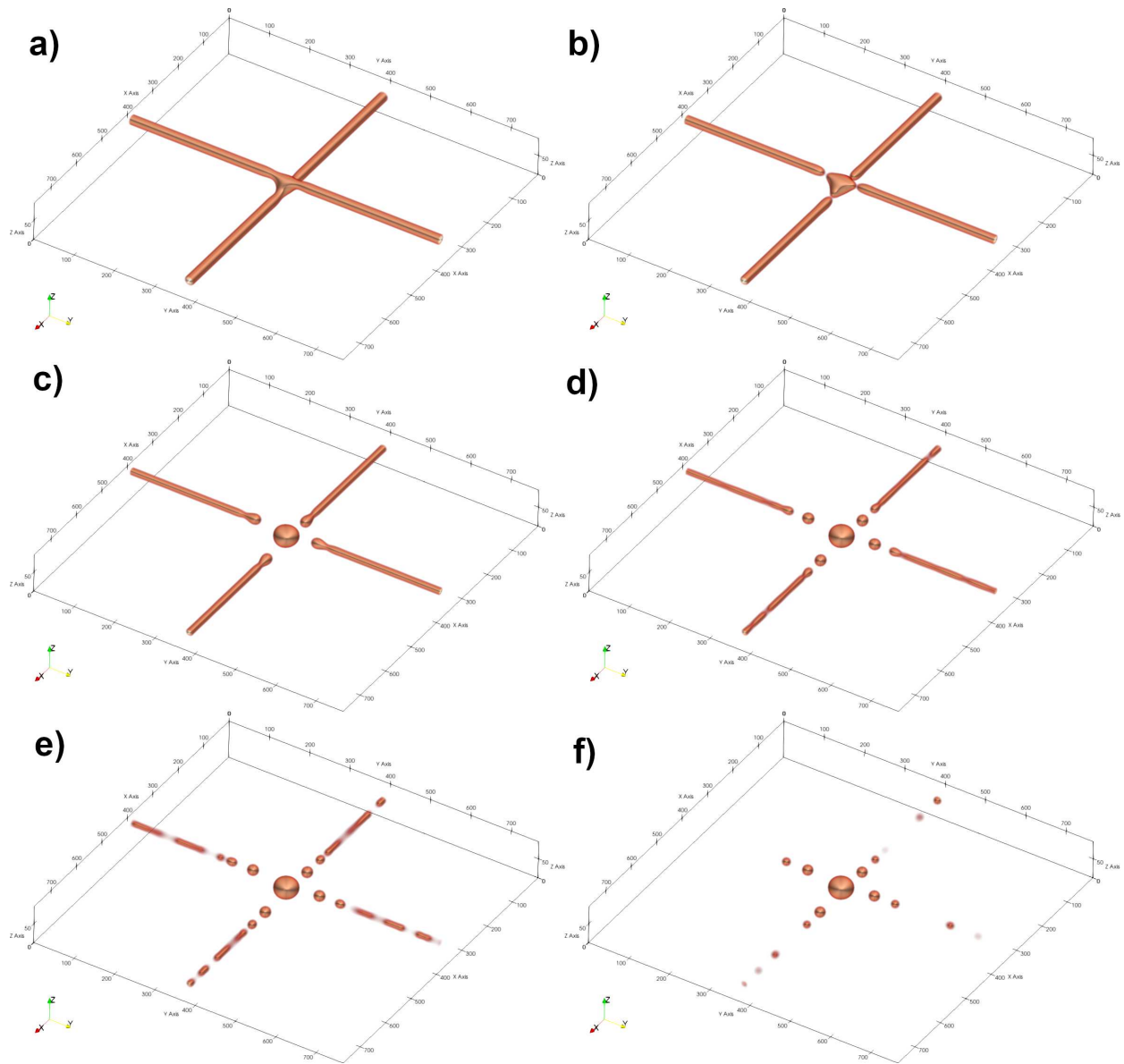


FIG. 4. Morphological evolution of two nanowires intersecting at 90° at different times: (a) 1000, (b) 1750, (c) 2500, (d) 2750, (e) 2800 and (f) 2900 time units. The video of the break-up is available as supplementary data.

a junction forms at the intersection (Fig. 4(a), corresponding to a (non-dimensional) time of 1000 units). The material accumulation at the junction leads to the break-up of the nanowire (Fig. 4(b), corresponding to a (non-dimensional) time of 1750 units). This, in turn, leads to subsequent break-up of the nanowire as seen in Fig. 4(c)-(e), corresponding to a (non-dimensional) times of 2500, 2750 and 2800 units. As can be seen from Fig. 4(f), corresponding to a (non-dimensional) time of 2900 units, the broken pieces of the nanowire coarsen due, primarily to, the difference in sizes

between the central particle and the others along the wire length.

After fragmentation of the junction, the free ends of the nanowire retract and subsequently break-up. After the break-up at the junction, the arms of the wire are similar to a single finite nanowire in their geometry. Hence, one can ask if their break-up is also similar to finite nanowires. As we can see, although the sequence of fragmentation is the same, the kinetics is not the same in these systems. In case of a single finite nanowire of radius 12, the first pinch-off event (ovulation) occurs at 2303 time units, the second pinch-off occurs at 2315, the third pinch-off occurs at 2666, and the fourth pinch-off occurs at 2680. Therefore, the first set of two pinch-off events are closely spaced because these events occur at the two free ends, and similarly for the next set of two pinch-off events which again occur at the free ends. In case of the 90° configuration, first fragmentation occurs at the junction at 1719 time units, and subsequently the second pinch-off event along the arm of nanowire occurs at 2549 units. Thus, in the presence of the junction, the time to first failure is faster as compared to a single, isolated finite nanowire.

In order to better understand the effect of orientation, in Fig. 5, we show the morphological evolution in the case of an angle of intersection of 45° between the two nanowires (of the same radii, namely, 12 units). In this case also, there is junction formation at the intersection; however, unlike the previous case where the contact between the nanowires is at a point, in this case, the contact between the two wires is along a line. Hence, the differences in curvatures at different points at the intersection lead to more material filling in at the sites which make smaller angle with the wire along the x -axis. Thus, when the central break-up takes place, the morphology of the central particle is not spherical; it is elongated and is aligned closer to (the infinite wire along) the x -axis. The subsequent break-ups and the coarsening are similar to the earlier case.

In Fig. 6 and Fig. 7, we show the morphological evolution for the cases of nanowires (of radii 12 units) which make angles of intersection of 30° and 60° , respectively. These morphologies are qualitatively similar to that in Fig. 5 in terms of the morphology of the central particle.

These microstructural features are in good agreement with experimental observations. For example, all the features noticed in the simulations above, namely, the formation of junction, the first break-up at the junction, and elongated central particle when the angle of intersection of wires is not 90° are seen in experiments – specifically, see the Figures 3 and 4 of Ref.³⁰. Interestingly, our simulation results also resemble nano-welds generated experimentally using different techniques like furnace annealing (Fig.3(c) of Ref.⁶⁹), and laser nano-welding of long Ag nanowires (Fig. 4 of Ref.¹). However, it is not clear to us if these welding are a result of local melting at the junction. In

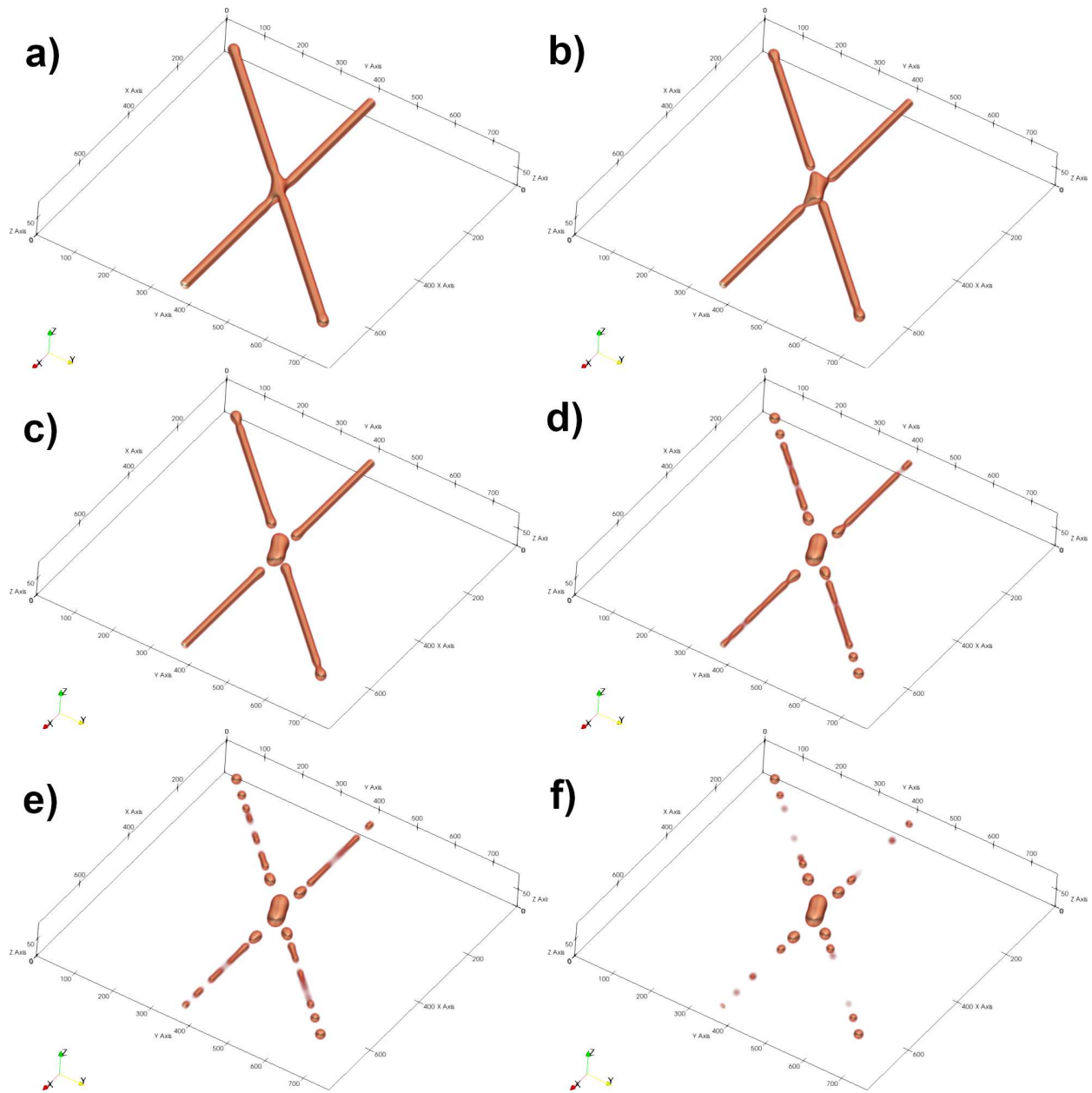


FIG. 5. Morphological evolution of two nanowires intersecting at 45° at different times: (a) 1000, (b) 2000, (c) 2250, (d) 2750, (e) 2800 and (f) 2900 time units. The video of the break-up is available as supplementary data.

our simulations, however, there is no local melting and all the morphological changes are through mass transport by enhanced surface diffusion.

Phase-field modelling has been used previously to simulate the sintering of Ag nanoparticles⁷⁰. The effect of local sintering at the junction of nanowires have also been studied using atomistic simulation methods, where it was observed that the nanowires undergo self-limiting rotation dur-

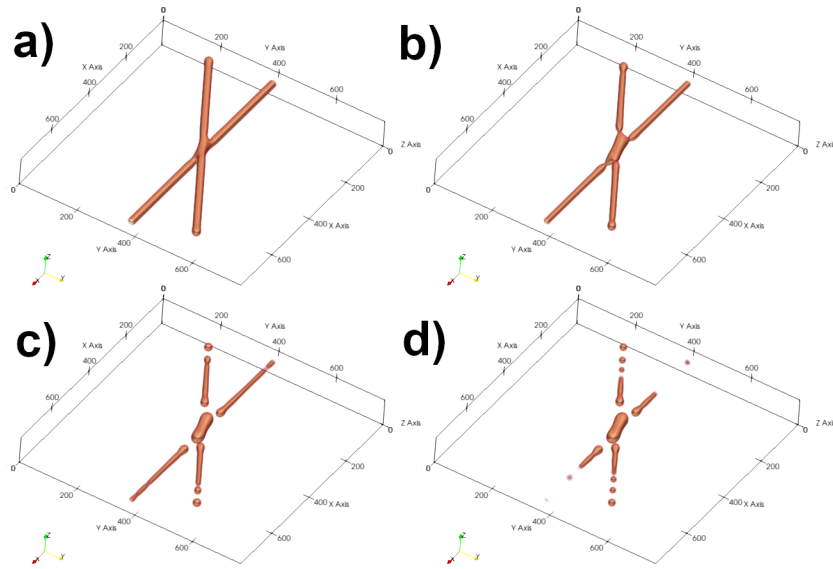


FIG. 6. Morphological evolution of two nanowires intersecting at 30° at different times: (a) 750, (b) 2125, (c) 2750, and (d) 2950 time units. The video of the break-up is available as supplementary data.

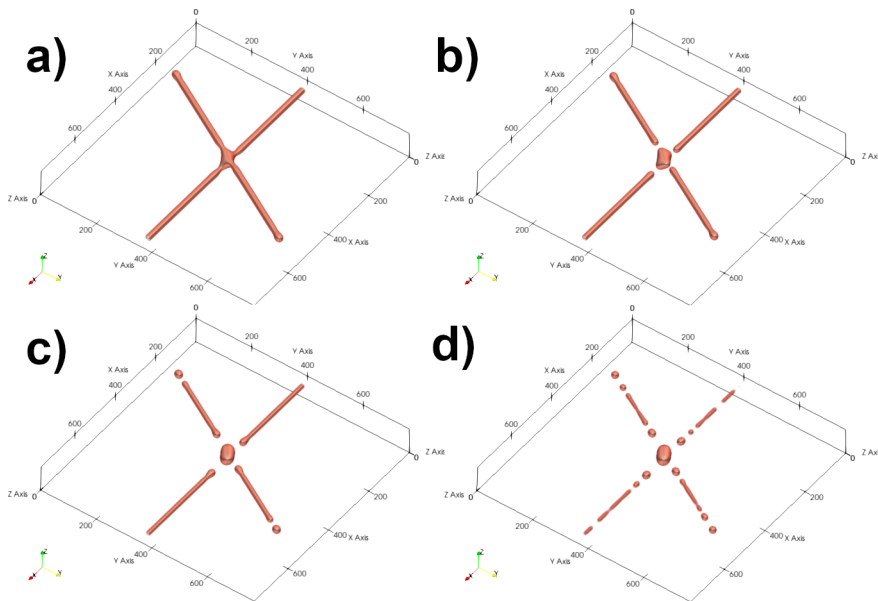


FIG. 7. Morphological evolution of two nanowires intersecting at 60° at different times: (a) 1500, (b) 2000, (c) 2500, and (d) 2800 time units. The video of the break-up is available as supplementary data.

ing neck growth, which is a result of complex interaction of surface diffusion and dislocation growth⁷¹. We also observe the nanowire junction break-up in all cases described above as a result of local sintering at the junctions of nanowires. In isolated nanowires, the primary cause of fragmentation is the Rayleigh instability. But, the presence of junctions lead to modification of

curvature and chemical potential in the intersection region, leading to junction formation followed by preferential break-up at the junctions.

Our simulation results are also in good agreement not only with the experimental results but also with the kinetic Monte Carlo simulation studies of Vigonski et al³⁰. They reported a similar observation of preferential fragmentation of nanowires initially at the junction. Vigonski et al, proposed that intersecting surfaces of nanowires act as sites of defects promoting atomic diffusion and attributed break-up at the junction primarily to the mechanism of diffusion of surface atoms. In this study, we show that the geometric factors in terms of the curvature leads to sintering at the junctions, of course, assisted by faster surface diffusion. Further, unlike the results from the Monte Carlo simulations, the phase-field model allow us to explore long time dynamics and morphological evolution such as the subsequent nanodot formation and the coarsening of the dots.

In order to better understand the junction formation and the subsequent break-up at the junctions, we have mapped the mean curvature and chemical potential in these systems. As shown by Nichols and Mullins¹², the surface movement in these systems is driven by the the mean curvature of the interface. In Fig. 8, we show the mean curvature ((a) and (b)) and chemical potential ((c) and (d)) maps for the 90° wire configuration, at the instant of break up and after the formation of nanodots. In this plot, the mean curvature is visualized as a colour map (at the order parameter isosurface of $c = 0.5$) overlaid on the nanowire assembly. The chemical potential is visualized as a colour map in a plane which cuts through the cross section of nanowires (the nanowires are superimposed for visual clarity). The colour maps for the chemical potential correspond to excess chemical potential above its mean value. Not surprisingly, the chemical potential maps have one-to-one correspondence with the mean curvature maps indicating that the driving forces for atomic diffusion at different regions of the nanowire assembly are due to the surface energy considerations.

In Fig. 9- 12, we show the mean curvature maps (in the first row). In all cases, as can be seen, initially, the high curvatures at the constrictions formed near the junction increase the chemical potential leading to higher atomic transport. Hence, atoms diffuse from these narrow regions towards the central nanoparticle and arms of the nanowires. Therefore, these constrictions get narrower finally causing detachment of nanowires from the junction. At this point, we wish to note that the saddle point, where the two principal curvatures assume values of opposite sign during the sintering of the nanowires at the junction is better seen in the Gaussian curvature maps of these morphologies as shown in the Supplementary Information.

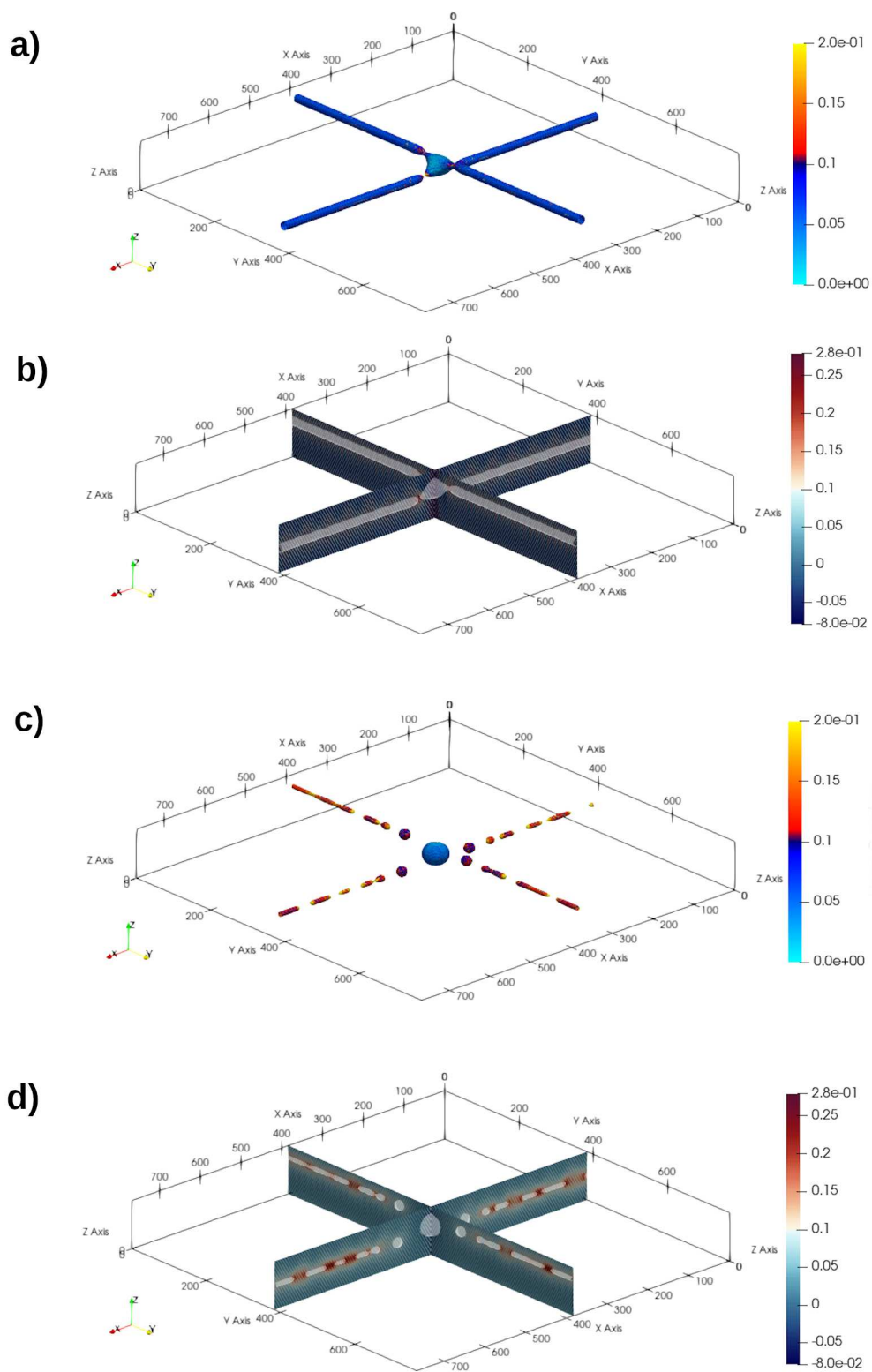


FIG. 8. Mean curvature maps at two different times (1700 and 2800 time unites) for the 90° configuration, along with the corresponding chemical potential maps.

Thereafter, the free ends of the nanowires retract due to high curvature at the tip of the broken junction. As these nanowire free ends retract, more matter accumulates and these tips get blunted. Subsequently these tips acquire a spherical shape and get detached; this mechanism is the same as observed in Rayleigh instability driven break-up. This process continues leading to formation of further constrictions along the arms of the nanowires, which are regions of higher chemical potential. This leads to subsequent formation of nanodots. These nanodots show a mean curvature of about 0.05 which occurs due to the spheroidisation of the nanoparticles – in order to reduce the (isotropic) interfacial energy.

The mean curvature is the mean of the two principal curvatures (κ_1 and κ_2) of the interface, one of which tries to stabilize the perturbation while the other tries to de-stabilize it. The interplay between the two principal curvatures which determines the evolution of the system is captured well using interfacial shape distribution (ISD) maps^{72–75}. The probability density of the principal curvatures are calculated, following Kwon et al⁷³ as

$$P(\kappa_1, \kappa_2) = \frac{A(\kappa_1, \kappa_2)}{A_{total}\Delta(\kappa)^2} \quad (13)$$

where $\Delta\kappa$ was taken as 0.005, $A(\kappa_1, \kappa_2)$ is the sum of area of all patches having principal curvatures between $\kappa_1, (\kappa_1 + \Delta\kappa)$ and $\kappa_2, (\kappa_2 + \Delta\kappa)$ and A_{total} is the total area of the interface. In Fig. 9-12, we show the ISD maps (in the second row) corresponding to the mean curvature maps shown above them.

In Fig.9, for example, we show the ISD maps for 90° case, at time steps of 100, 1000 and 2800 respectively, below the corresponding wire morphologies. The maximum value of probability density in all ISD maps reported is fixed at 100, to get a better resolution of the smaller values. Initially, there is a higher density along the $\kappa_1 = 0$ line, which corresponds to the larger fraction of cylindrical regions in the morphology, where one of the principal curvatures will be zero. The points in the $\kappa_1 < 0, \kappa_2 > 0$ regions correspond to the saddle shapes formed at the intersection of the two nanowires. These points are more pronounced at $t = 1000$ where the constrictions at the intersection become more pronounced. It is clear that the sign of the two curvatures in this region are opposite, which leads to a negative sign of the Gaussian curvature, making it a metric to identify the saddle shaped regions; as indicated above, the Gaussian curvature maps for all configurations have been provided in the Supplementary Information. The loss of material from the saddle shaped regions result in the break-up of the wire and the formation of nanodots, which evolve to be spherical in shape. At $t = 2800$ there is a large density of points in the $\kappa_1 > 0, \kappa_2 > 0$

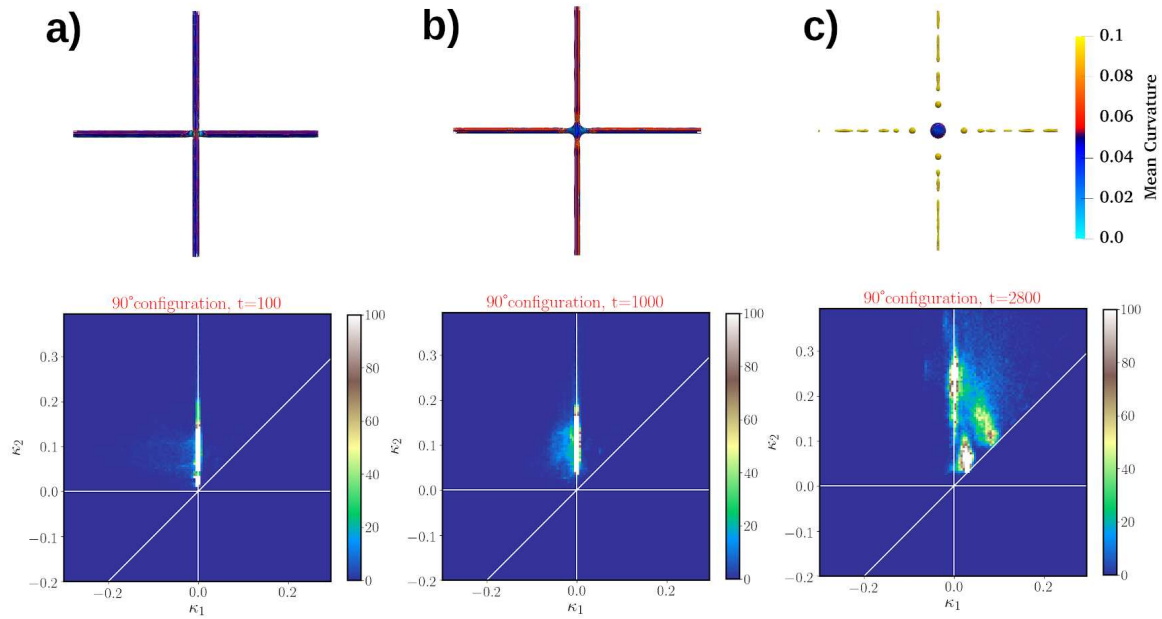


FIG. 9. The maps of mean curvature (top row) and the ISD maps (bottom row) for the 90° wire configuration at timesteps (a) 100, (b) 1000 and (c) 2800 respectively. The mean curvature maps show the morphology of the wires corresponding to the ISD map. The upper limit of probability density for the colour map has been fixed at 100 to resolve the smaller values.

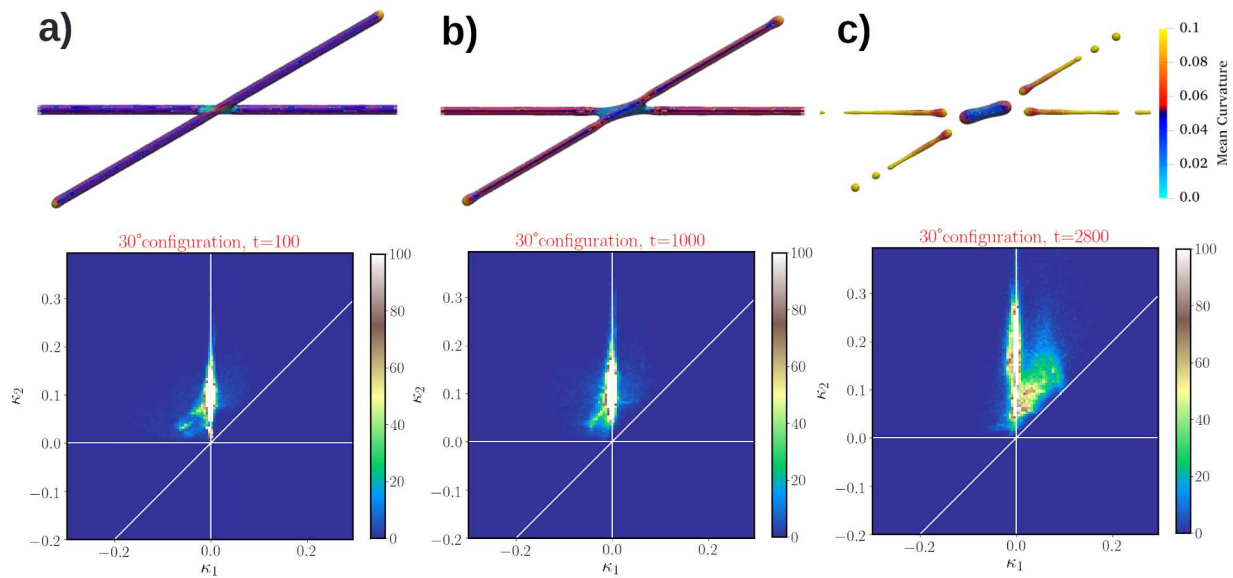


FIG. 10. The maps of mean curvature (top row) and the ISD maps (bottom row) for the 30° wire configuration at timesteps (a) 100, (b) 1000 and (c) 2800 respectively.

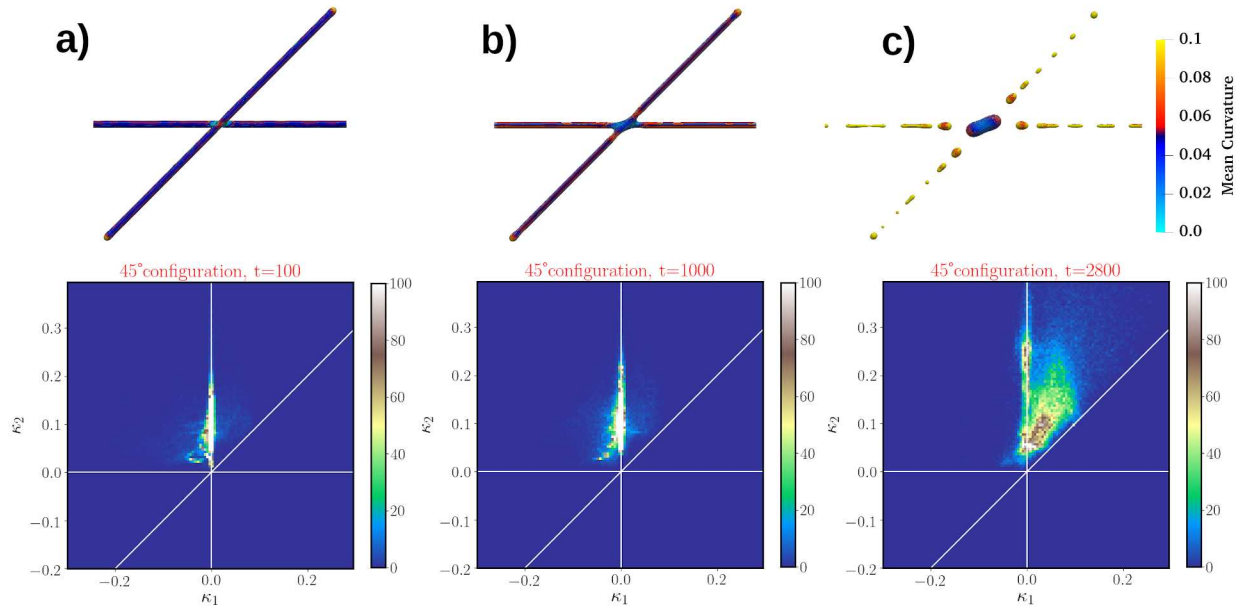


FIG. 11. The maps of mean curvature (top row) and the ISD maps (bottom row) for the 45° wire configuration at timesteps (a) 100, (b) 1000 and (c) 2800 respectively.

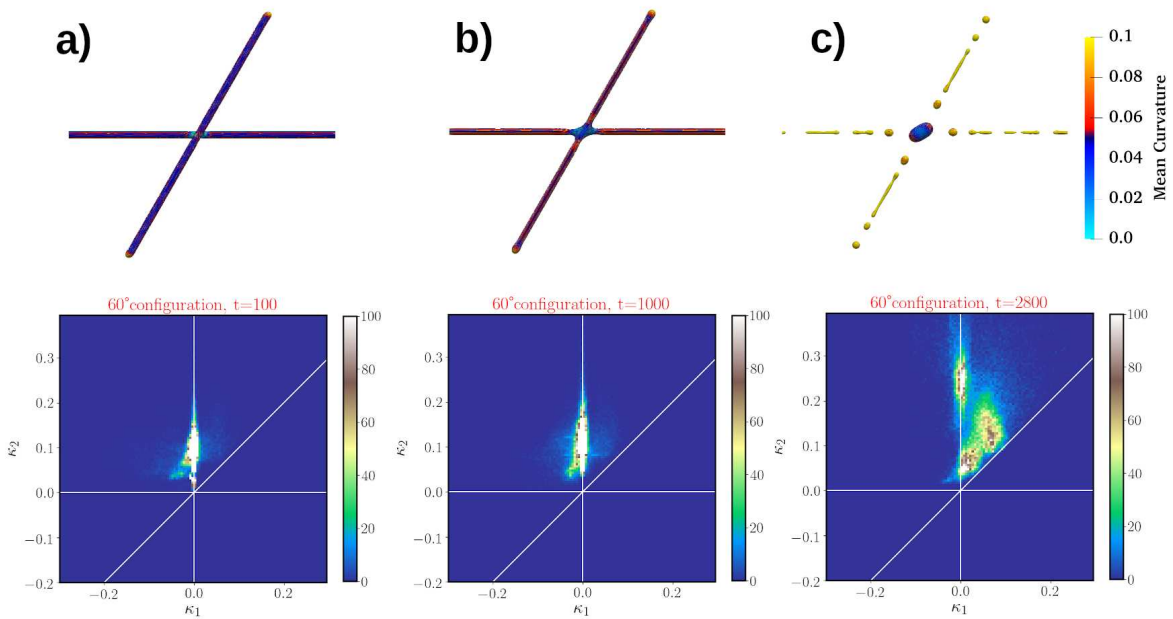


FIG. 12. The maps of mean curvature (top row) and the ISD maps (bottom row) for the 60° wire configuration at timesteps (a) 100, (b) 1000 and (c) 2800 respectively.

domain, corresponding to the convex surfaces. Two patches near the $\kappa_1 = \kappa_2$ line correspond to the near-spherical nanodots of different sizes, formed after the wire break-up. As the wire breaks up, the density of points at the $\kappa_1 = 0$ line reduces due to the smaller fraction of cylindrical region in the microstructure.

The ISD maps for the 30°, 45° and 60° configurations have also been made in Fig.10, Fig.11 and Fig.12 respectively. The underlying trend in these cases are also the same as that of 90° configuration. However, the increased overlap of the wires at the junctions for the angular configurations causes a higher density in the $\kappa_1 < 0$, $\kappa_2 > 0$ region of the map. This is due to the zipping of the two wires at the junction, resulting in a larger fraction of saddle shaped regions as compared to the 90° case. This is most pronounced in the 30° case, and becomes less and less pronounced for the 45° and 60° cases. As the wire breaks-up and starts to disintegrate, the density of points in the convex region ($\kappa_1 > 0$, $\kappa_2 > 0$) increases for all cases.

The angle between the nanowires does not affect the sequence of the nanowire break-up; the first fragmentation always occurs at the junction; but, it does affect the break-up kinetics. The time to first break-up (at the junction) is calculated for different orientations, and plotted in Fig. 13. Here, we have assumed that there is a break-up at the junction if two or more of the arms at a junction (consisting of four arms) detach. The data points are obtained from a set of three different simulations for each configuration (that is, by using three different seed values of pseudo-random number generator). It is observed that the system is relatively more stable as the acute angle between the nanowires decrease. The time to first junction break-up is highest for the 30° configuration system, and the least for 90° configuration system, when only the effect of relative wire orientation is considered in isolation. This observation can be correlated with the average distance between nearest nanodots from the central nanoparticle along the two nanowires, formed subsequently after the junction break-up (values given in Table II). From the values presented in Table II, it can be inferred that the average separation between the nanodots from the central nanoparticle along the two wires increases as the angle between the nanowires decrease. These values were calculated by averaging the results from three different set of simulations. The correlation between time to first junction break-up and average separation between the nanodots from the junction center can be explained with the mean curvature maps; as the angle between the nanowire decrease, the curvature increases at the junction which leads to enhanced atomic transport in between the two wires. Therefore, more material accumulates at the central agglomerate before constriction occurs at the junction, leading to nanowire junction break-up. For this reason, the central nanopar-

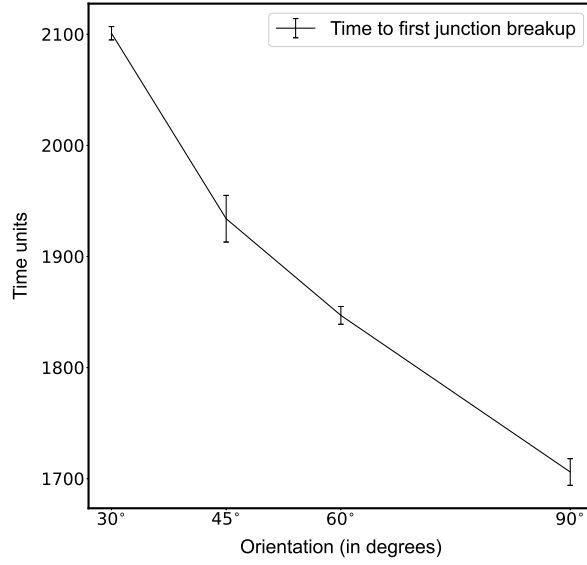


FIG. 13. Plot showing the dependence of time to first break-up at the junction on the relative wire orientation. The line connecting the data points is drawn only as a guide to the eye.

| Wire configuration | Distance along wire 1 | Distance along wire 2 |
|---------------------------|------------------------------|------------------------------|
| 30° configuration | 110.9 ± 0.4 | 111.5 ± 0.8 |
| 45° configuration | 94.1 ± 0.9 | 93.9 ± 0.6 |
| 60° configuration | 87 ± 0 | 85.3 ± 1.4 |
| 90° configuration | 83 ± 0 | 83 ± 0 |

TABLE II. Average distance of first nanodots from the central nanoparticle (wire 1 corresponds to the infinite length nanowire at the bottom, and wire 2 corresponds to the finite length inclined nanowire on top of the infinite length nanowire).

particle acquires an ellipsoidal shape as the angle between nanowire is reduced. The end result is the junction break-up substantially delayed along with the particles being placed afar from the center of the junction.

| Wire configuration | Time to first junction break-up |
|-------------------------------------|---------------------------------|
| $R_1 = 12, R_2 = 12$ | 1706 ± 12 |
| $R_1 = 12, R_2 = 14$ | 1623 ± 12 |
| $R_1 = 12, R_2 = 16$ | 1622 ± 10 |
| $R_1 = 14, R_2 = 14$ | 4000 ± 5 |
| $R_1 = 14, R_2 = 16$ | 3907 ± 15 |
| $R_1 = 16, R_2 = 16$ | 8142 ± 14 |
| 4-junction ($R_1 = 12, R_2 = 12$) | 1694 ± 9 |
| 9-junction ($R_1 = 12, R_2 = 12$) | 1691 ± 6 |

TABLE III. Time units to first break-up at the junctions for different configurations.

C. Effect of relative wire diameter

It has been observed experimentally that there is on average about 25% variation in the diameter of the fabricated metallic nanowires²⁰. Therefore, in order to study the effect of relative variation in diameters of the nanowires, we use three different assemblies of nanowires in 90° configuration, with initial radii of $R_1, R_2 = 12, 14, 16$. We study the three different combinations of radii —the first combination with $R_1 = 14, R_2 = 16$, the second combination with $R_1 = 12, R_2 = 14$, and the final combination with $R_1 = 12, R_2 = 16$; with the relative radius variations of 14%, 17%, and 33%, respectively. We have carried out a set of three different simulations for each case, and the average from these simulations are presented here.

It is observed that for all three combinations, the nanowires with smaller radius breaks up at the junction and the central agglomerate becomes part of the larger radius nanowires. The time to first junction break-up (values given in Table III) within a given margin of error is dependent primarily on the radius of the smaller diameter nanowire. Having said that, the difference in the radii of the nanowires has a small but definite effect on kinetics. The kinetics when the radii are different is slightly faster than when the radii are the same; for example, for the cases of $R_1 = 12, R_2 = 14$ and $R_1 = 12, R_2 = 16$ are slightly faster than $R_1 = R_2 = 12$ case.

We have summarised in Fig.14 the data given in Table III. We have used the 90° configuration for $R_1, R_2 = 14$ and $R_1, R_2 = 16$ and compare it with the 90° case with $R_1, R_2 = 12$. From Fig.14, it can be observed that the time to first junction break-up increases drastically as the radius of the

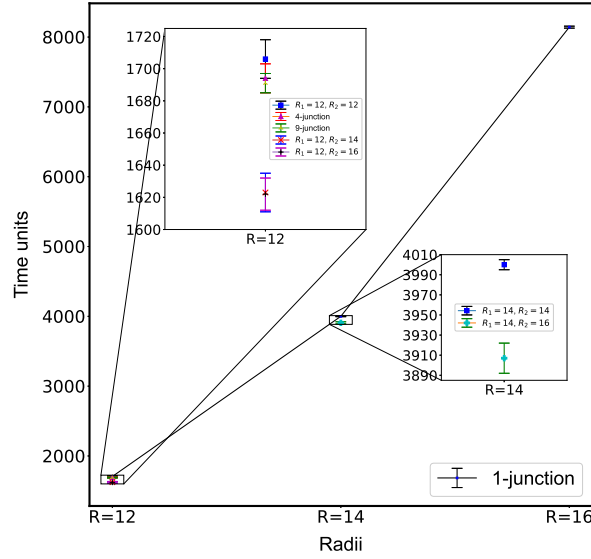


FIG. 14. Plot showing the dependence of time to first break-up at the junctions on the relative wire radii. The values for time to first junction break-up for 4-junction and 9-junction grid, as well different radii combinations are given for comparison (the magnified inset is provided for better visibility). The line connecting the data points is drawn only as a guide to the eye.

nanowires is increased. This difference, in our opinion, is related to the reduction in driving force due to increasing size of the nanowires which leads to smaller driving forces and the fact that in our simulations while the radii are increased, the inter-junction distance is maintained a constant.

D. Effect of the density of junctions

During fabrication of nanowires, it is seldom possible to fabricate a nanowire in isolation. In most practical cases, they are fabricated in large numbers with the nanowire network resembling structures best approximated as a grid pattern⁷⁶. It has been observed that local sintering at the junction of nanowires has drastic effects on the optimization of electrical and optical properties of the nanowire networks^{7,10,69,77}. The network density (no of junctions in close proximity) also plays a role in optical transmittance of the assembly. Therefore, we have carried out systematic study of nanowire assemblies consisting of grids with 1, 4, and 9 junctions in the simulation cell. Since the 4 and 9-junctions behave qualitatively the same, we only show the results for the 9-junction configuration in Fig.15. In all the three cases, we observe the first fragmentation of the

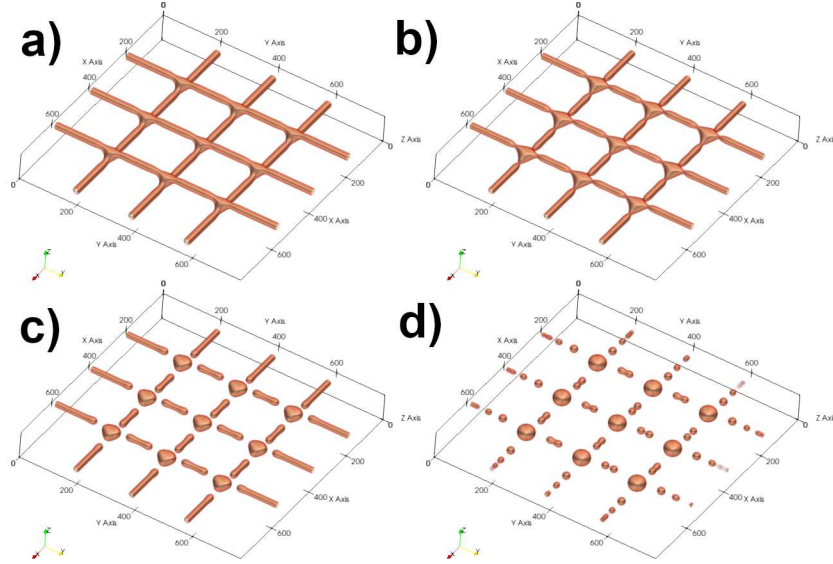


FIG. 15. Morphological evolution of nanowires with 9 junctions in the simulation cell at different times. The video of the break-up is available as supplementary data.

nanowires to occur at the junctions; however, the specific junction at which the first detachment occurs is stochastic in nature. We track the time to first junction break-up for all the three cases, and correlate the junction break-up kinetics with the number of junctions in close proximity, the values of which are given in Table III. It is observed that within the given margin of error, there is no substantial difference between the time to first junction break-up. Therefore, close proximity of the junctions does not effect the the break-up kinetics of individual junctions in the network. The kinetics remains unaffected, but the morphological evolution plays a role in the network electrical resistance which falls during annealing to reach a stable minima followed by an abrupt rise, as reported in^{7,10}. This experimental observation can be directly correlated with the morphological evolution of the nanowire assembly of the 9-junction grid as seen in Fig.15(a) to (d). As the sintering occurs, the network resistance is expected to decrease continuously due to junction formation, followed by an abrupt increase due to fragmentation at the junctions.

IV. CHARACTERIZATION OF THE CENTRAL NANOPARTICLE MORPHOLOGY

In this section, we analyse the morphology of the central nanoparticles formed as a result of junction break-up. The nanoparticles which are formed as a result of detachment of nanowires from the junction assume different morphologies. These morphologies are primarily dependent

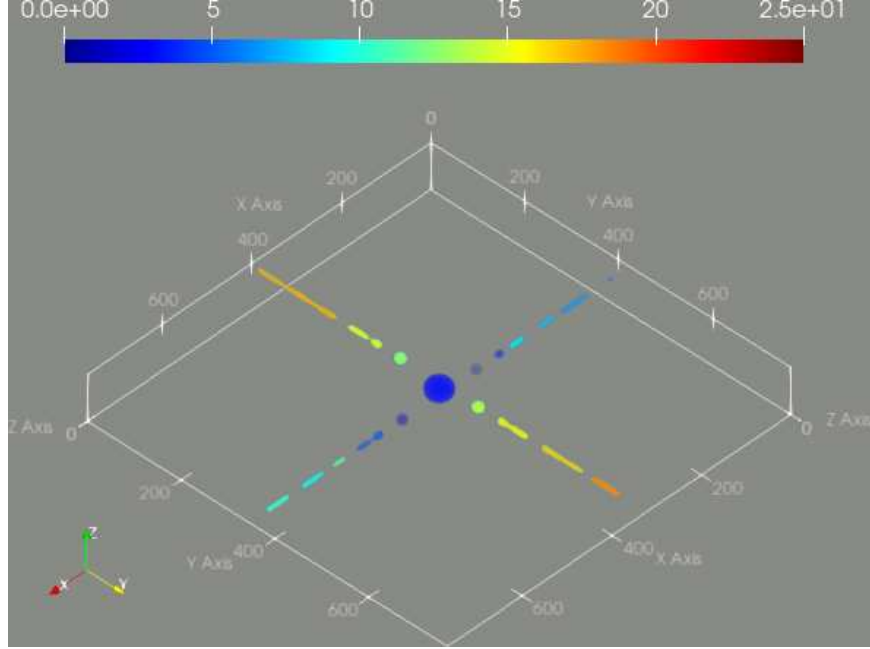


FIG. 16. Labelled clusters for the 90° configuration. Each cluster is denoted by a specific colour from the corresponding colormap shown in the image.

on the angle of intersection between the nanowires. In order to quantify the morphologies of the non-spherical nanoparticles at the centres (formed as a result of the break-up of the junctions), we first use a 3D implementation of the Hoshen-Kopelman algorithm⁷⁸ and label the different fragments. The central nanoparticles is isolated using the algorithm by doing an analysis of the microstructures at a time which is later than the junction break-up time for that configuration. As an example, we show the labelled clusters for the 90° configuration in Fig. 16. Similar labelled clusters for other configurations are shown in the Supplementary Information.

After labelling the clusters, we extract the data points corresponding to the label of the central nanoparticle and subsequently characterize its morphology. The isolated nanoparticles for four different configurations are shown in Fig. 17. It is clearly seen that as the initial angle between the nanowires decreases, the central nanoparticle diverges significantly from spherical shape. The central nanoparticle assumes an oblate spheroidal shape for the 90° configuration, and it diverges from sphericity as the angle is decreased. For the 30° configuration, it assumes a nearly ellipsoidal shape. We also calculate the cluster size (nanoparticle volume) for all four configurations as shown in Fig 18.

We can make the characterization of central nanoparticle quantitative using the moment of

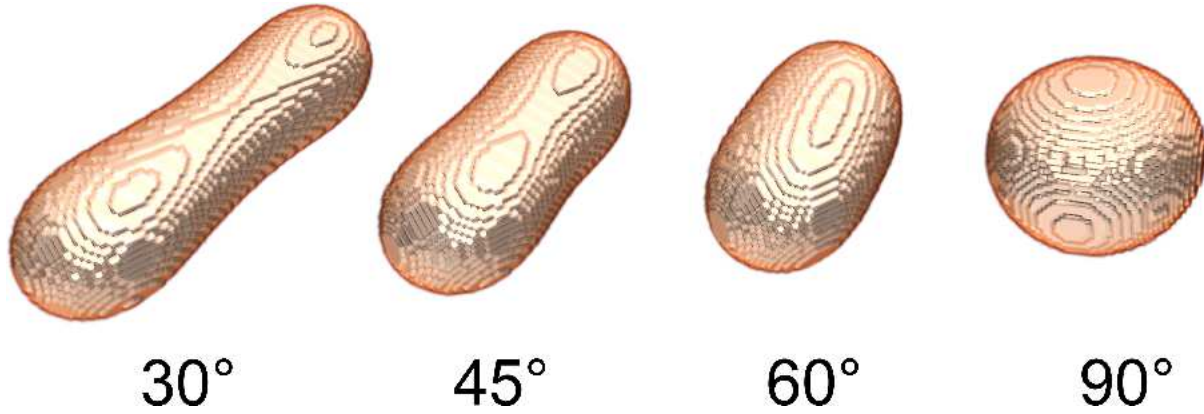


FIG. 17. Nanoparticle morphologies of the isolated central nanoparticles for four different configurations.

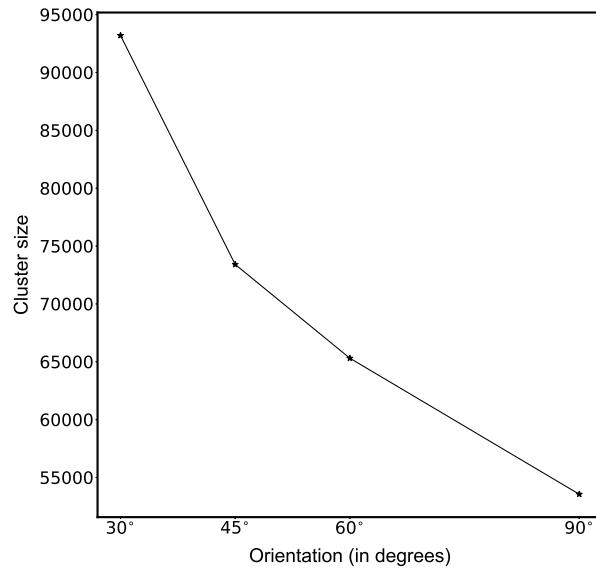


FIG. 18. Cluster size for the four different configurations.

inertia tensor (See Appendix B) of the particles. The moment of inertia tensor (calculated about the center of mass of the nanoparticle) is a real, symmetric tensor. We obtain the three eigenvalues and eigenvectors of this tensor. The three eigenvectors give the directions of the three principal axes of the nanoparticle (corresponding to the three axes of rotation), and, the three eigenvalues describe the distribution of mass around the three corresponding principal axes.

In the schematic of an ellipsoidal body shown in Fig. 19, the principal axis (P) makes an angle of α with the x-axis, β with the y-axis, and γ with the z-axis, respectively. The three principal axes are denoted by P1, P2 and P3, respectively. We use this notation convention for the angles

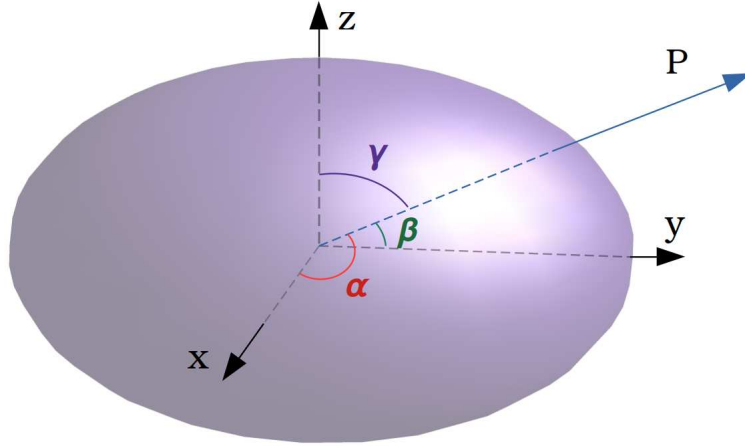


FIG. 19. Schematic of an ellipsoidal body with its three principal axes is shown. One of the principal axis (P-axis) makes an angle of α with the x-axis, β with the y-axis, and γ with the z-axis.

and report the results of principal axis calculation in Table IV.

TABLE IV. Angles the three principal axes make with the coordinate axes for all four configurations.

| Configuration | principal Axes | α | β | γ |
|-------------------|----------------|----------|---------|----------|
| 30° configuration | P1 | 14.74 | 75.26 | 89.92 |
| | P2 | 75.26 | 14.26 | 89.29 |
| | P3 | 89.89 | 89.28 | 0.72 |
| 45° configuration | P1 | 22.02 | 67.98 | 89.95 |
| | P2 | 67.99 | 22.01 | 89.64 |
| | P3 | 89.82 | 89.65 | 0.35 |
| 60° configuration | P1 | 30.70 | 59.30 | 89.86 |
| | P2 | 59.30 | 30.70 | 89.77 |
| | P3 | 90.00 | 89.73 | 0.27 |
| 90° configuration | P1 | 83.34 | 6.67 | 89.95 |
| | P2 | 6.66 | 83.33 | 89.57 |
| | P3 | 89.55 | 89.80 | 0.45 |

From the values of angles α , β , and γ presented in Table IV, it is observed that two principal axes P1, and P2 are aligned approximately along the acute and obtuse angle bisectors of the respec-

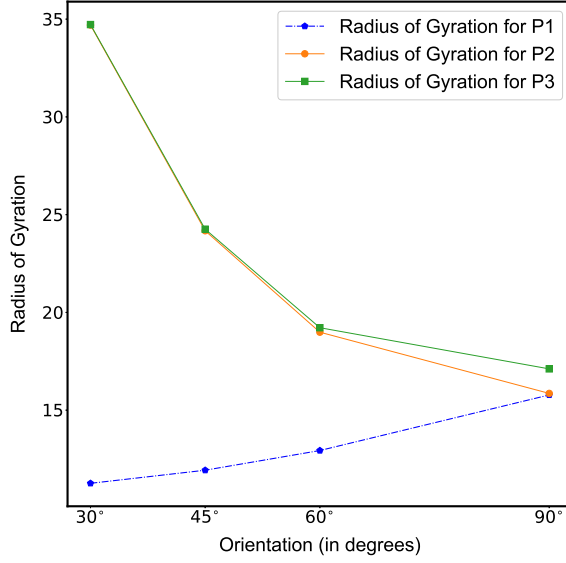


FIG. 20. The three radius of gyration corresponding to the three eigenvalues of inertia matrix along the three principal axis for all four configurations.

tive configuration (in all cases except when the wires are perpendicular to each other). The third principal axis (P3) is aligned along the z-axis for all four configurations (perpendicular to the plane of the nanowires). Therefore, it can be inferred that after the junction break-up, the nanoparticles possess rotation axes aligned along the angle bisectors of the initial angle between the nanowires. Subsequently, we also calculate the three radii of gyration corresponding to the three eigenvalues of the inertia matrix corresponding to the three principal axes (details in the appendix). The radii of gyration values are presented in Fig. 20. We denote R1 as the radius of gyration corresponding to the eigenvalue of the inertia tensor for principal axis P1. Similarly, R2 corresponds to P2, and R3 corresponds to P3. From the plot, it is observed that the radii of gyrations R2 and R3 increase with decrease in the angle between nanowires. These radii of gyration to correspond to the principal axes perpendicular to the semi-major axis of the nanoparticles (i.e., along the z-axis and perpendicular to it along the y-axis). The other radius of gyration R1 corresponds to the principal axis along the x-axis (direction of elongation). This trend, along with the observation that the difference between the two radii of gyrations (P2 and P3) and the third radius (P1) increases with decrease in angle between the nanowires indicate that the nanoparticles diverge from sphericity.

V. CONCLUSIONS

In this paper, we have shown, using a phase field model (implemented in both 2- and 3-D), that at the intersection of nanowires, sintering (curvature driven material flow) leads to the formation of junctions. These junctions act the initiators of nanowire break-up; the subsequent break-ups take place due to Rayleigh instability at the arms away from these junctions. The fragments coarsen due to the differences in sizes. Further, the effect of various parameters on the junction break-up can be summarised as follows:

- The radii of the nanowires play a key role in the kinetics; smaller the radii, faster is the kinetics. The kinetics is determined primarily by the radius of the smaller of the two nanowires that intersect.
- The angle of intersection is the next key parameter; smaller the angle of intersection, slower the break-up at the junction. This is primarily due to the non-spherical morphology (and, relatively larger size) of the junction.
- The above two observations in terms of the size difference and the effect of intersection angle can be rationalised in terms of the mean curvatures (and, hence chemical potential) maps.
- The density of intersections in the simulation cell have very little or no effect on the kinetics.

The mean curvatures and ISD maps based on the two principal curvatures can be used to rationalise the nanowire fragmentation process. Further, the shapes of the fragmented nanoparticles can be analysed quantitatively using the moment of inertia tensor and its eigenvalues and eigenvectors. Thus, phase-field models, and the simulation results based on them could be of use and importance in the study of stability of nanowire nets and their morphological evolution at long time scales.

SUPPLEMENTARY MATERIAL

See supplementary material for animations of nanowire junction break-up for different configurations.

ACKNOWLEDGMENTS

We thank the following high performance computing facilities for making the computational resources available to us: (i) Dendrite and Space-Time, IIT Bombay, (ii) Spinode – the DST-FIST HPC facility, Department of Metallurgical Engineering and Materials Science, IIT Bombay, and (iii) and C-DAC, Pune.

DATA AVAILABILITY STATEMENT

The codes used for the simulations are available at the following GitHub repository:
<https://github.com/abhinavroy1999/nanowire-fragmentation-code>.

The data that support the findings of this study are also available from the corresponding author upon reasonable request.

Appendix A: Effect of interfacial energy anisotropy

Experimentally, it is known that single-crystalline and poly-crystalline metallic nanowires possess faceted morphologies and this preference in surface orientation is attributed to surface energy anisotropy²¹. The diverse effects of surface energy anisotropy in FCC metallic nanowires have been investigated using Monte Carlo models¹⁸. It has been reported that Au nanowires develop facets as a result surface diffusion in order to minimize the surface energy³⁰.

We note that for studying Rayleigh instability in these anisotropic systems, 3-D simulations are essential. Even though our formulation is valid for 3-D and we have a numerical implementation for 3-D, given the highly non-linear nature of the evolution equations, and the variable mobility (to account for the faster surface diffusion), the time steps are extremely small and hence the system has to be evolved to much higher time steps to observe break-up. Hence, at the moment, we are not able to carry out 3D simulations in reasonable amounts of time. However, efforts of parallel implementation of these models are in progress in our group; such implementations, when available, will help us study 3-D anisotropic systems. Hence, in this section we present some preliminary 2D simulation results on the effect of anisotropy in surface energy of the nanowires on morphological change and junction break-up.

We study two different configurations with nanowires oriented at an angle of 90° and 45° . In this case, we use the wire radius of value $R_1, R_2 = 6$. The values of the isotropic and anisotropic

contributions to the gradient energy coefficient, namely γ_I and γ_A are given in Table I. The values are chosen such that the $\langle 11 \rangle$ direction is energetically more favoured than the $\langle 10 \rangle$ direction, i.e., the ratio of the interfacial energies (anisotropy ratio) $R_\sigma = \frac{\sigma_{\langle 11 \rangle}}{\sigma_{\langle 10 \rangle}}$ is chosen to be less than unity. Hence, it is expected that the morphological evolution of the nanowires will lead to surfaces on the nanowires whose surface normal vectors are along the energetically favoured $\langle 11 \rangle$ direction. As noted above, the Δt values are to be chosen appropriately in this case in order to maintain the stability of the stiff numerical scheme.

The 2D microstructure maps for the 90° case is given in Fig.21, and the maps for the 45° are given in Fig.22. From the microstructure maps, it is evident that for the 45° case, the wire aligned along the energetically favoured direction is stabilized, whereas the wire along the less energetically favoured direction undergoes change in morphology. The morphological change in the 90° case is such that constrictions develop at regular intervals so as to give rise to surfaces with the surface normal vectors aligned parallel to the $\langle 11 \rangle$ direction. In both the cases, we observe that the fragmentation of the nanowires occurs initially at the junction, followed by break-up along the nanowire arms. This observation leads to the conclusion that the order in which the nanowires fragment is independent of the anisotropy in interfacial energy, with the first break-up occurring at the junction. After the fragmentation the nanowires retract, and it is expected that in case of 90° configuration, further fragmentation will occur along the nanowire arms. Further, in spite of the overall higher interfacial energy in the anisotropic cases, note that the kinetics of break-up is, relatively speaking, slower. This is primarily due to the stabilization of certain interfaces, we believe.

In the past, theoretical treatment of surface energy anisotropy^{14,50} predicted that the weak axisymmetric perturbations will be stabilized depending on the nature of derivatives of interfacial energy (particularly the second derivative). Our phase field results above can be thought of as a validation of these predictions and an attempt to correlate the stability criteria with the underlying crystallographic symmetry. Here again, our simulation results are in good agreement with the kinetic Monte Carlo simulation results obtained by Vigonski et al.³⁰, where they aligned the Au nanowires along $\langle 110 \rangle$ direction and observed the fragmentation to occur initially at the junction. In their simulation, the nanowires initially having $\{110\}$ facets decomposed to more stable $\{111\}$ and $\{100\}$ facets. Our phase-field simulation results also reproduce same results; the nanowires develop energetically stable facets before undergoing fragmentation.

To summarise, the preliminary 2-D simulations results indicate that in the case of systems with

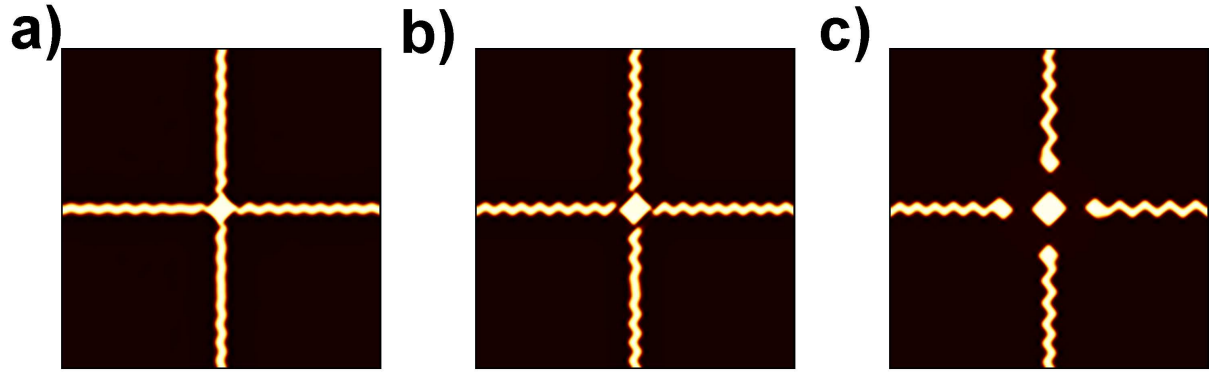


FIG. 21. Morphological evolution of two nanowires with cubic anisotropic interfacial free energy, and, intersecting at 90° at different times: (a) 2000, (b) 3000 and (c) 20000 time units. The $\langle 11 \rangle$ interfaces are preferred over $\langle 10 \rangle$ interfaces.

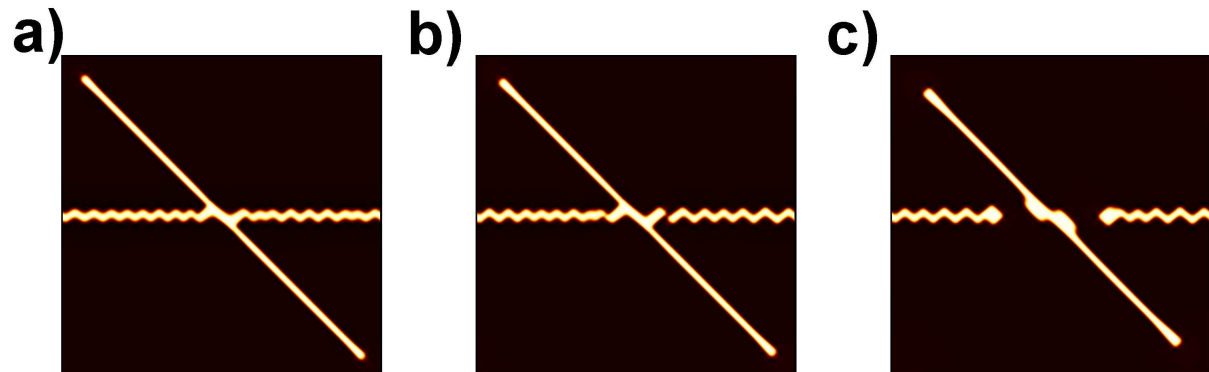


FIG. 22. Morphological evolution of two nanowires with cubic anisotropic interfacial free energy, and, intersecting at 45° at different times: (a) 5000, (b) 8000 and (c) 20000 time units. The $\langle 11 \rangle$ interfaces are preferred over $\langle 10 \rangle$ interfaces.

surface energy anisotropy, wires with surfaces along the energetically favourable directions are unconditionally stable; and the anisotropy in surface energy has a strong effect on kinetics. These results indicate that 3-D simulations of nanowires with interfacial anisotropy could be interesting.

Appendix B: Moment of inertia tensor

We define the moment of inertia matrix consisting of the nine components of the corresponding tensor as follows:

$$I = \begin{pmatrix} I_{xx} & -I_{xy} & -I_{xz} \\ -I_{xy} & I_{yy} & -I_{yz} \\ -I_{xz} & -I_{yz} & I_{zz} \end{pmatrix} \quad (\text{B1})$$

where, the components of the real symmetric inertia matrix are defined as:

$$\begin{aligned} I_{xx} &= \sum (y^2 + z^2) dm \\ I_{yy} &= \sum (x^2 + z^2) dm \\ I_{zz} &= \sum (x^2 + y^2) dm \\ I_{xy} &= I_{yx} = \sum (xy) dm \\ I_{yz} &= I_{zy} = \sum (yz) dm \\ I_{xz} &= I_{zx} = \sum (xz) dm \end{aligned} \quad (\text{B2})$$

In these terms, dm is the mass of each individual particle constituting the body. We assign a value of unity to dm .

Appendix C: Radius of gyration

The standard eigenvalue problem for real symmetric matrix is given as follows:

$$\begin{pmatrix} I_{xx} & -I_{xy} & -I_{xz} \\ -I_{xy} & I_{yy} & -I_{yz} \\ -I_{xz} & -I_{yz} & I_{zz} \end{pmatrix} \begin{pmatrix} V_x \\ V_y \\ V_z \end{pmatrix} = \begin{pmatrix} I_0 & 0 & 0 \\ 0 & I_0 & 0 \\ 0 & 0 & I_0 \end{pmatrix} \begin{pmatrix} V_x \\ V_y \\ V_z \end{pmatrix} \quad (\text{C1})$$

where, (V_x, V_y, V_z) are components of the eigenvectors. After solving the above eigenvalue problem, we obtain three eigenvalues $I_0 = I_1, I_2, I_3$, and three eigenvectors corresponding to the three eigenvalues. We define the radius of gyration corresponding to these three eigenvalues of the moment of inertia matrix as:

$$\begin{aligned} R1 &= \sqrt{\frac{I_1}{M}} \\ R2 &= \sqrt{\frac{I_2}{M}} \\ R3 &= \sqrt{\frac{I_3}{M}} \end{aligned} \quad (\text{C2})$$

where, M is the mass of the body whose inertia tensor is calculated.

REFERENCES

- ¹J. Lee, P. Lee, H. Lee, D. Lee, S. S. Lee, and S. H. Ko, *Nanoscale* **4**, 6408 (2012).
- ²T. Sannicolo, M. Lagrange, A. Cabos, C. Celle, J. P. Simonato, and D. Bellet, *Small* **12**, 6052 (2016).
- ³S. Lee, J. Jang, T. Park, Y. M. Park, J. S. Park, Y. K. Kim, H. K. Lee, E. C. Jeon, D. K. Lee, B. Ahn, and C. H. Chung, *ACS Applied Materials and Interfaces* **12**, 6169 (2020).
- ⁴L. Gonzalez-Garcia, J. H. Maurer, B. Reiser, I. Kanelidis, and T. Kraus, *Procedia Engineering* **141**, 152 (2016).
- ⁵O. Vazquez-Mena, T. Sannomiya, L. G. Villanueva, J. Voros, and J. Brugger, *ACS Nano* **5**, 844 (2011).
- ⁶T. B. Song, Y. S. Rim, F. Liu, B. Bob, S. Ye, Y. T. Hsieh, and Y. Yang, *ACS Applied Materials and Interfaces* **7**, 24601 (2015).
- ⁷D. P. Langley, M. Lagrange, G. Giusti, C. Jiménez, Y. Bréchet, N. D. Nguyen, and D. Bellet, *Nanoscale* **6**, 13535 (2014).
- ⁸H. S. Shin, J. Yu, and J. Y. Song, *Applied Physics Letters* **91**, 173106 (2007).
- ⁹M. Rauber, F. Muench, M. E. Toimil-Molares, and W. Ensinger, *Nanotechnology* **23** (2012).
- ¹⁰M. Lagrange, D. P. Langley, G. Giusti, C. Jiménez, Y. Bréchet, and D. Bellet, *Nanoscale* **7**, 17410 (2015).
- ¹¹L. Rayleigh, *Proceedings of the London Mathematical Society* **s1-10**, 4 (1878).
- ¹²F. A. Nichols and W. W. Mullins, *Journal of Applied Physics* **36**, 1826 (1965).
- ¹³Q. Ma, *Acta Materialia* **46**, 1669 (1998).
- ¹⁴J. Cahn, *Scripta Metallurgica* **13**, 1069 (1979).
- ¹⁵J. S. Stölken and A. M. Glaeser, *Scripta Metallurgica et Materialia* **27**, 449 (1992).
- ¹⁶K. F. Gurski and G. B. McFadden, *Proceedings of the Royal Society A: Mathematical, Physical and Engineering Sciences* **459**, 2575 (2003).
- ¹⁷G. H. Kim and C. V. Thompson, *Acta Materialia* **84**, 190 (2015).
- ¹⁸V. N. Gorshkov, V. V. Tereshchuk, and P. Sareh, *CrystEngComm* **22**, 2601 (2020).
- ¹⁹M. E. Molares, A. G. Balogh, T. W. Cornelius, R. Neumann, and C. Trautmann, *Applied Physics Letters* **85**, 5337 (2004).

- ²⁰S. Karim, M. E. Toimil-Molares, A. G. Balogh, W. Ensinger, T. W. Cornelius, E. U. Khan, and R. Neumann, *Nanotechnology* **17**, 5954 (2006).
- ²¹S. Karim, M. E. Toimil-Molares, W. Ensinger, A. G. Balogh, T. W. Cornelius, E. U. Khan, and R. Neumann, *Journal of Physics D: Applied Physics* **40**, 3767 (2007).
- ²²X. H. Huang, Z. Y. Zhan, X. Wang, Z. Zhang, G. Z. Xing, D. L. Guo, D. P. Leusink, L. X. Zheng, and T. Wu, *Applied Physics Letters* **97**, 1 (2010).
- ²³K. R. Beavers, N. E. Marotta, and L. A. Bottomley, *Chemistry of Materials* **22**, 2184 (2010).
- ²⁴C. P. Hsiung, H. W. Liao, J. Y. Gan, T. B. Wu, J. C. Hwang, F. Chen, and M. J. Tsai, *ACS Nano* **4**, 5414 (2010).
- ²⁵H. Oh, J. Lee, and M. Lee, *Applied Surface Science* **427**, 65 (2018).
- ²⁶F. M. Kolb, H. Hofmeister, M. Zacharias, and U. Gösele, *Applied Physics A* **80**, 1405 (2005).
- ²⁷M. Bechelany, J. L. Riesterer, A. Brioude, D. Cornu, and P. Miele, *CrystEngComm* **14**, 7744 (2012).
- ²⁸J. Bürki and C. A. Stafford, *Applied Physics A* **81**, 1519 (2005).
- ²⁹F. Kassubek, C. A. Stafford, H. Grabert, and R. E. Goldstein, *Nonlinearity* **14**, 167 (2001).
- ³⁰S. Vigonski, V. Jansson, S. Vlassov, B. Polyakov, E. Baibuz, S. Oras, A. Aabloo, F. Djurabekova, and V. Zadin, *Nanotechnology* **29**, 015704 (2017).
- ³¹Z. Xue, M. Xu, Y. Zhao, J. Wang, X. Jiang, L. Yu, J. Wang, J. Xu, Y. Shi, K. Chen, and P. R. i Cabarrocas, *Nature Communications* **7**, 1 (2016).
- ³²Y. Zhu, J. Chen, T. Wan, S. Peng, S. Huang, Y. Jiang, S. Li, and D. Chu, *ACS Applied Electronic Materials* **1**, 1275 (2019).
- ³³A. S. Barnard, *Reports on Progress in Physics* **73** (2010).
- ³⁴L.-Q. Chen, *Annual Review of Materials Research* **32**, 113 (2002).
- ³⁵I. Steinbach and O. Shchyglo, *Current Opinion in Solid State and Materials Science* **15**, 87 (2011).
- ³⁶A. M. Lacasta, A. Hernandez-Machado, and J. M. Sancho, *Physical Review B* **45**, 5276 (1992).
- ³⁷A. J. Bray and C. L. Emmott, *Physical Review B* **52**, 685 (1995).
- ³⁸S. Puri, A. J. Bray, and J. L. Lebowitz, *Physical Review E* **56**, 758 (1997).
- ³⁹J. Zhu, L.-Q. Chen, J. Shen, and V. Tikare, *Physical Review E* **60**, 3564 (1999).
- ⁴⁰P. A. Geslin, M. Buchet, T. Wada, and H. Kato, *Physical Review Materials* **3**, 1 (2019).
- ⁴¹M. Salvalaglio, M. Selch, A. Voigt, and S. M. Wise, *Mathematical Methods in the Applied Sciences* **44**, 5406 (2020).

- ⁴²W. B. Andrews, K. L. Elder, P. W. Voorhees, and K. Thornton, *Physical Review Materials* **4**, 1 (2020).
- ⁴³C. Joshi, T. A. Abinandanan, and A. Choudhury, *Acta Materialia* **109**, 286 (2016).
- ⁴⁴C. Joshi, T. A. Abinandanan, R. Mukherjee, and A. Choudhury, *Computational Materials Science* **139**, 75 (2017).
- ⁴⁵R. Mukherjee, T. Chakrabarti, E. A. Anumol, T. A. Abinandanan, and N. Ravishankar, *ACS Nano* **5**, 2700 (2011).
- ⁴⁶T. Chakrabarti, N. Verma, and S. Manna, *Materials and Design* **119**, 425 (2017).
- ⁴⁷J. M. Debierre, A. Karma, F. Celestini, and R. Gu erin, *Physical Review E* **68**, 1 (2003).
- ⁴⁸Y. Ji, B. Ghaffari, M. Li, and L. Q. Chen, *Computational Materials Science* **151**, 84 (2018).
- ⁴⁹T. A. Abinandanan and F. Haider, *Philosophical Magazine A* **81**, 2457 (2001).
- ⁵⁰N. Wang, *Phase-field studies of materials interfaces*, Ph.D Thesis, Northeastern University (2011).
- ⁵¹A. Roy, E. S. Nani, A. Lahiri, and M. P. Gururajan, *Philosophical Magazine* **97**, 2705 (2017).
- ⁵²J. W. Cahn and J. E. Hilliard, *The Journal of Chemical Physics* **28**, 258 (1958).
- ⁵³M. Dziwnik, A. M unch, and B. Wagner, *Nonlinearity* **30**, 1465 (2017).
- ⁵⁴W. Jiang, W. Bao, C. V. Thompson, and D. J. Srolovitz, *Acta Materialia* **60**, 5578 (2012).
- ⁵⁵M. Verma and R. Mukherjee, *Journal of Alloys and Compounds* **835**, 155163 (2020).
- ⁵⁶F. Cheynis, E. Bussmann, F. Leroy, T. Passanante, and P. M uller, *International Journal of Nanotechnology* **9**, 396 (2012).
- ⁵⁷S. Liu and J. L. Plawsky, *Langmuir* **33**, 14066 (2017).
- ⁵⁸K. Liu, I. Berbezier, L. Favre, A. Ronda, T. David, M. Abbarchi, P. Gaillard, T. Frisch, B. Croset, and J.-N. Aqua, *Physical Review Materials* **3**, 023403 (2019).
- ⁵⁹J. W. Cahn, C. M. Elliott, and A. Novick-Cohen, *European Journal of Applied Mathematics* **7**, 287 (1996).
- ⁶⁰C. Gugenberger, R. Spatschek, and K. Kassner, *Physical Review E* **78**, 1 (2008), 0711.1809.
- ⁶¹M. Dziwnik, *Proceedings in Applied Mathematics and Mechanics* **19**, 29 (2019).
- ⁶²J. Shin, Y. Choi, and J. Kim, *Mathematical Problems in Engineering* **2019** (2019).
- ⁶³P. W. Hoffrogge, A. Mukherjee, E. S. Nani, P. G. K. Amos, F. Wang, D. Schneider, and B. Nestler, *Physical Review E* **103**, 1 (2021).
- ⁶⁴L.-Q. Chen and J. Shen, *Computer Physics Communications* **108**, 147 (1998).
- ⁶⁵M. Frigo and S. G. Johnson, *Proceedings of the IEEE* **93**, 216 (2005).

- ⁶⁶A. Roy and M. P. Gururajan, PTM 2015 - Proceedings of the International Conference on Solid-Solid Phase Transformations in Inorganic Materials 2015 , 325 (2015).
- ⁶⁷W. W. Mullins, Journal of Applied Physics **28**, 333 (1957).
- ⁶⁸M. Gururajan, Elastic Inhomogeneity Effects on Microstructures, Ph.D. thesis, Indian Institute of Science Bangalore (2006).
- ⁶⁹A. T. Bellew, H. G. Manning, C. Gomes da Rocha, M. S. Ferreira, and J. J. Boland, ACS Nano **9**, 11422 (2015).
- ⁷⁰K. Chockalingam, V. G. Kouznetsova, O. van der Sluis, and M. G. Geers, Computer Methods in Applied Mechanics and Engineering **312**, 492 (2016).
- ⁷¹M. N. Jahangir, H. Devaraj, and R. Malhotra, Journal of Physical Chemistry C **124**, 19849 (2020).
- ⁷²R. Mendoza, J. Alkemper, and P. Voorhees, Metallurgical and Materials Transactions A **34**, 481 (2003).
- ⁷³Y. Kwon, K. Thornton, and P. Voorhees, Philosophical Magazine **90**, 317 (2010).
- ⁷⁴C.-L. Park, P. W. Voorhees, and K. Thornton, Computational Materials Science **85**, 46 (2014).
- ⁷⁵C.-L. Park, J. Gibbs, P. Voorhees, and K. Thornton, Acta Materialia **132**, 13 (2017).
- ⁷⁶D. Li, T. Han, and H. Ruan, ACS Omega **3**, 7191 (2018).
- ⁷⁷Y. Hu, C. Liang, X. Sun, J. Zheng, J. Duan, and X. Zhuang, Nanomaterials **9** (2019).
- ⁷⁸J. Hoshen and R. Kopelman, Physical Review B **14**, 3438 (1976).